Controlled Fabrication of Photoactive Copper Oxide–Cobalt Oxide Nanowire Heterostructures for Efficient Phenol Photodegradation

Wenwu Shi and Nitin Chopra*

Department of Metallurgical and Materials Engineering, Center for Materials for Information Technology (MINT), Box 870202, The University of Alabama, Tuscaloosa, Alabama 35487, United States

Ⓢ Supporting Information

ABSTRACT: Fabrication of oxide nanowire heterostructures with controlled morphology, interface, and phase purity is critical for high-efficiency and low-cost photocatalysis. Here, we have studied the formation of copper oxide–cobalt nanowire heterostructures by sputtering and subsequent air annealing to result in cobalt oxide (Co_3O_4)-coated CuO nanowires. This approach allowed fabrication of standing nanowire heterostructures with tunable compositions and morphologies. The vertically standing CuO nanowires were synthesized in a thermal growth method. The shell growth kinetics of Co and Co_3O_4 on CuO nanowires, morphological evolution of the shell, and nanowire self-shadowing effects were found to be strongly dependent on sputtering duration, air-annealing conditions, and alignment of CuO nanowires. Finite element method (FEM) analysis indicated that alignment and stiffness of CuO–Co nanowire heterostructures greatly influenced the nanomechanical aspects such as von Mises equivalent stress distribution and bending of nanowire heterostructures during the Co deposition process. This fundamental knowledge was critical for the morphological control of Co and Co_3O_4 on CuO nanowires with desired interfaces and a uniform coating. Band gap energies and phenol photodegradation capability of CuO–Co_3O_4 nanowire heterostructures were studied as a function of Co_3O_4 morphology. Multiple absorption edges and band gap tailings were observed for these heterostructures, indicating photoactivity from visible to UV range. A polycrystalline Co_3O_4 shell on CuO nanowires showed the best photodegradation performance (efficiency ~50–90%) in a low-powered UV or visible light illumination with a sacrificial agent (H_2O_2). An anomalously high efficiency (~67.5%) observed under visible light without sacrificial agent for CuO nanowires coated with thin (~5.6 nm) Co_3O_4 shell and nanoparticles was especially interesting. Such photoactive heterostructures demonstrate unique sacrificial agent-free, robust, and efficient photocatalysts promising for organic decontamination and environmental remediation.

KEYWORDS: nanowire, nanoparticles, polycrystalline shell, finite element method, nanomechanics, electron microscopy, Raman spectroscopy, photocatalysis
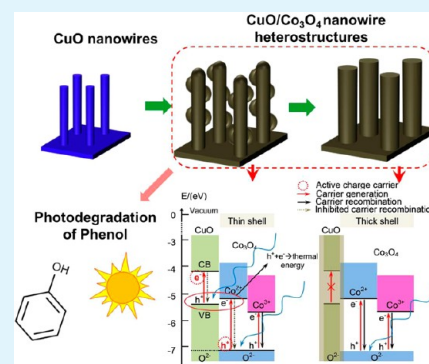
1. INTRODUCTION

Bottom-up and/or top-down growth methods that allow easy manipulation of chemical composition and morphology of heterostructured 1-D nanostructures, such as core/shell nanowires, are a critical fabrication challenge.[1−5] The interfaces in such heterostructured and semiconducting nanowires (e.g., oxides, nitrides, and phosphides)[6−8] facilitate rapid charge transport[9] and exhibit unique electronic and photonic properties.[10] For example, core/shell nanowire heterostructures can allow for multilevel light–matter interaction with charge transport directed across the thin shell (radially) and rapid charge conduction through the core (longitudinally).[2,4,11] Such interaction is not possible with single-component nanowires or by physically mixing of materials[12] and makes nanowire heterostructures extremely attractive for water splitting, CO_2 photocatalytic reduction,[13] and solar energy harvesting.[4,9,14]

Nanowire heterostructures composed of oxides are of interest for a wide array of applications and can be synthesized using various methods including solution synthesis, gas phase growth (physical vapor deposition (PVD) and chemical vapor deposition (CVD)), air oxidation, and flame synthesis.[15−22] Typically, a core nanowire is coated with a layer of a second component with specific thickness and composition.[16,17,19,23] The solution routes have their advantages; they are simple, cheap, and scalable.[23,24] Dispersion of metal salts onto nanowires and subsequent thermal decomposition has shown potential to result in nanowire heterostructures organized in vertical arrays or horizontally suspended architectures.[24,25] Flame synthesis is a scalable approach for fabricating oxide nanowire heterostructures, but the challenge is to control the growth of uniform and thin oxide shells around core nanowires.[21] Gas phase techniques are well-suited but necessitate understanding materials-specific thermodynamics and processes to avoid formation of continuous films on the surfaces.[26] Although atomic level control of stoichiometric ratio and perfect site-selective deposition can be obtained for

nanowire heterostructures using CVD and pulsed laser deposition (PLD),[27,28] high cost and low throughput remains a problem. As compared to the above-mentioned methods, sputter deposition is a conventional, scalable, and cost-effective technique for assembling oxide nanostructures (e.g., nanowires) on the substrate, without patterning or using templates.[29,30] This approach also holds significant promise for developing complex nanowire heterostructures.[31]

Among various oxides, CuO and Co_3O_4 photocatalysts are of particular interest.[14,24,25,32,33] These oxides are stable and can result in narrow to wide band gap energies depending on their dimensions/morphologies.[6,14] Such oxide-based photocatalysts are also considered as potential replacements for precious metals.[34] In addition, semiconducting CuO nanowires can be grown in a simple and environment-friendly method.[35] They can survive multiple processing steps and have the ability to combine with other material systems. All of these characteristics make them interesting base materials for nanowire heterostructures.[21,35,36] The authors recently reported that CuO nanowire–Co_3O_4 nanoparticle heterostructures have unique photoactivity under a low-power (8 W) illumination lamp with organic dye degradation efficiencies as high as 17% compared to pristine CuO nanowires.[24] The synthesis approach for these heterostructures involved wet-chemical coating of CuO nanowires with cobalt salt and thermal decomposition of the latter to obtain Co_3O_4 nanoparticles.[24] However, this approach limited the growth of Co_3O_4 in the form of well-dispersed nanoparticles or islands on the CuO nanowire surface. Furthermore, such a processing method does not necessarily allow for manipulation of Cu and Co content in the heterostructures. Thus, the promising photocatalytic behavior of the CuO–Co_3O_4 system and the need for simpler synthesis routes make it critical to develop a completely dry processing method with excellent tunability of heterostructure morphology and composition. Correlation of the latter aspects with photocatalytic activity would allow systematic exploitation of quantum confinement and surface effects in these heterostructured nanowires.[37] Such knowledge will help improve and control photocatalytic performance of the heterostructures due to the synergistic effects of phases, material components, interfaces, and morphologies.

Here, we study the morphological and structural evolution of CuO–Co_3O_4 nanowire heterostructures in a surfactant-free and dry processing approach that combines a line-of-sight sputter deposition method with a thermal annealing process. It is hypothesized that controlled structure, morphology, and interfaces in CuO–Co_3O_4 nanowire heterostructures will lead to precise tuning of their band gap energies and photocatalytic ability. This study emphasizes the growth mechanisms, morphological evolution, structural integrity, and nanomechanical aspects of nanowire heterostructures. In addition, the photocatalytic behavior of fabricated CuO–Co_3O_4 nanowire heterostructures is studied for phenol photodegradation in UV and visible light illumination with or without sacrificial agent (H_2O_2). To the best of the authors' knowledge, such a fabrication route and detailed understanding of the formation, stability, and photoactivity of nanowire heterostructures composed of oxides of copper and cobalt is not reported until now.

2. EXPERIMENTAL SECTION

2.1. Materials, Methods, and Characterization. Copper foil (0.254 mm thick, 99.9%), hydrogen peroxide (35%), and phenol (99+

%) were purchased from Alfa Aesar (Ward Hill, MA). Nitric acid (HNO_3, 69.5%) and hydrochloric acid (HCl, 37%) were purchased from Fisher Scientific (Pittsburgh, PA). Deionized (DI, 18.1 MΩ·cm) water was obtained using a Barnstead International DI water system (E-pure D4641). Quartz cuvette for photodegradation and UV experiments was purchased from Ocean Optics (Dunedin, FL). UV and visible light lamps were obtained from Fisher Scientific (Pittsburgh, PA). Box furnace used for the annealing process was purchased from MTI Inc. (Redmond, CA). Microscopic characterization and energy-dispersive X-ray spectroscopy (EDS) were performed using a field emission scanning electron microscopy (FE-SEM, JEOL-7000, equipped with Oxford EDX detector) and a transmission electron microscope (TEM, Tecnai FEI-20). X-ray diffraction (XRD) patterns were collected with a Philips diffractometer (XRG 3100, Cu Kα radiation, 35 mA and 40 kV). In order to eliminate copper substrate, all films were scratched and grounded into powder before loading into the diffractometer. The Raman spectra and depth profiling were recorded using Senterra micro-Raman spectrometer (Bruker Optics, Woodlands, TX) equipped with a 785 nm laser and a motorized stage with 0.1 μm positioning accuracy in the z-direction. Laser power of 10 mW was utilized to minimize the thermal effect of the laser. UV–vis–NIR spectroscopy was performed using an Ocean Optics USB 4000 spectrometer (Dunedin, FL) with a reflection/ backscattering probe. The reference spectrum was collected using polytetrafluoroethylene (PTFE) as a reflective standard. Sputter deposition was performed using an AJA International (North Situate, MA) Orion 3 sputtering system, and the high-purity Co target (99.99%, 3 mm thickness, 2 in. diameter) was bought from the same.

2.2. Synthesis of CuO–Co Nanowire Heterostructures, CuO–Co_3O_4 Nanowire Heterostructures, and Co_3O_4 Nanotubes. A copper foil (99.9%, 0.254 mm thick, 2 × 2 cm²) was immersed into diluted HNO_3 solution (1:2 v/v HNO_3/H_2O) for 15 s to remove the native oxide layer. The cleaned copper foil was washed with copious amounts of deionized (DI) water and dried. Subsequently, the substrate was placed in a ceramic crucible and heated at 410 °C in a box furnace in air. After 6 h, the furnace was cooled naturally and a black film of vertically aligned CuO nanowires was formed on the copper foil.[32,35] These nanowires were further sputtered with Co films using a high-purity Co target to result in standing CuO–Co nanowire heterostructures. The sputtering target-to-sample distance was kept constant at ~10 cm. The base pressure of the chamber was lower than 2×10^{-7} Torr, and deposition pressure was maintained at 3 mTorr with 25.1 sccm Ar flow. Before opening the target shutter and actual deposition on the substrate, the target was presputtered for at least 2 min to eliminate native oxide layers. In regard to manipulating the morphology of the coated Co on CuO nanowires, the effect of sputtering time was studied (1–50 min). After sputtering, the chamber was vented with dry N_2 flow (~5 psi). A control sample was prepared by sputter deposition of Co film on the cleaned Si/SiO_2 wafer, and this aided in estimating Co film thickness and sputter deposition rate/flux for calibration purposes. Film thickness of this control sample was measured by a profilometer (Veeco, Plainview, NY). The standing CuO–Co nanowire heterostructures were formed as a film (black film) on the base copper substrate and were gently peeled off from the latter. This black film was loaded into a ceramic boat and air-annealed at 520 °C for different durations to study the formation of standing CuO–Co_3O_4 nanowire heterostructures. A detailed parametric study was conducted as listed in Table S1 (Supporting Information) to understand the role of sputtered Co morphology and thickness in the morphological evolution of Co_3O_4 on CuO nanowires as a function of Co sputtering time and annealing duration. As a next step, sample #3B (Table S1) was utilized to fabricate Co_3O_4 nanotubes. Diluted HCl (2:5 v/v 35% HCl/H_2O) was used to selectively remove CuO nanowires from the core. Approximately, 1 mL of diluted acid solution was dropped into a cleaned watch glass containing CuO–Co_3O_4 nanowire heterostructures. The etching process was allowed for 2 min. After this duration, the remaining Co_3O_4 nanotubes were collected and rigorously washed with DI water several times using a centrifuge (~6000 rpm) for 1 min.
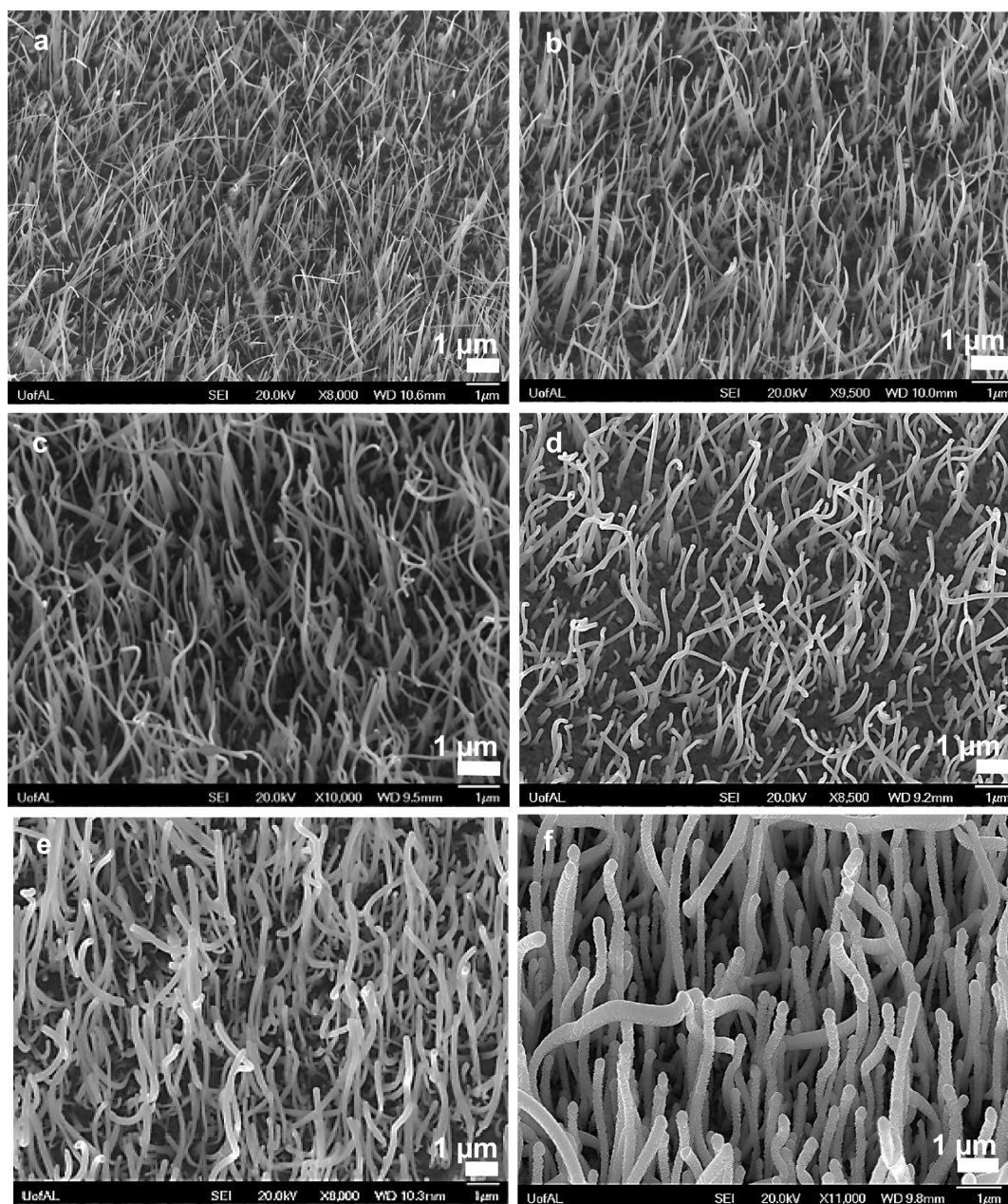
Figure 1. SEM images of standing CuO−Co nanowire heterostructures fabricated after Co sputter deposition for (a) 1 min, (b) 5 min, (c) 10 min, (d) 20 min, (e) 30 min, and (f) 50 min (scale bar: 1 μm, and samples were tilted at 20° in SEM).

The washing process was continued until the pH of the solution was neutral.

2.3. Phenol Photodegradation Study Using CuO−Co$_3$O$_4$ Nanowire Heterostructures. In order to test the photocatalytic abilities of the CuO−Co$_3$O$_4$ nanowire heterostructures, phenol photodegradation experiments were conducted and various parameters were studied. These include illumination wavelength (UV and visible), presence and absence of sacrificial agent (H$_2$O$_2$), and morphology of Co$_3$O$_4$ coating on CuO nanowires (samples #1B−6B, Table S1). The degradation experiments were performed inside a quartz cuvette (1 cm × 1 cm × 4 cm), and for all of the experiments, the ratio of photocatalyst amount to phenol volume is kept constant at ∼1 g/L. Approximately, 3 mg of photocatalyst (as-produced CuO nanowires, Co$_3$O$_4$ nanotubes, or CuO−Co$_3$O$_4$ nanowire heterostructures) was dispersed and briefly sonicated (1 min) in 3 mL of phenol (0.2 mM). This was followed by addition of ∼12 μL of H$_2$O$_2$ (37%). An illumination lamp (UV source: centered at 254 nm, 8 W) was placed above the cuvette, and the solution was gently stirred. UV−vis spectroscopy was utilized to measure the concentration of phenol, and the spectrum was collected every 2 min. Photodegradation efficiency (η) was calculated using the following equation:

$$\eta = [1 - C_t/C_0] \times 100 \qquad (1)$$

where C_0 is the initial phenol concentration and C_t is the concentration of phenol at time $t = t$. Similar photocatalytic degradation experiments were conducted for white light illumination (centered at 580 nm, 8 W), with and without sacrificial agent (H$_2$O$_2$), where the catalyst/phenol solution ratio (1 g/L) was kept constant. It has to be noted that, for visible light illumination experiments, the photodegradation with H$_2$O$_2$ was carried out in the phenol concentration of ∼0.2 mM. In the case of photodegradation without H$_2$O$_2$, the phenol concentration was ∼0.1 mM. The sampled solution for visible light experiments was analyzed every 30 or 60 min using UV−vis spectroscopy. The kinetics of phenol photodegradation was also studied.
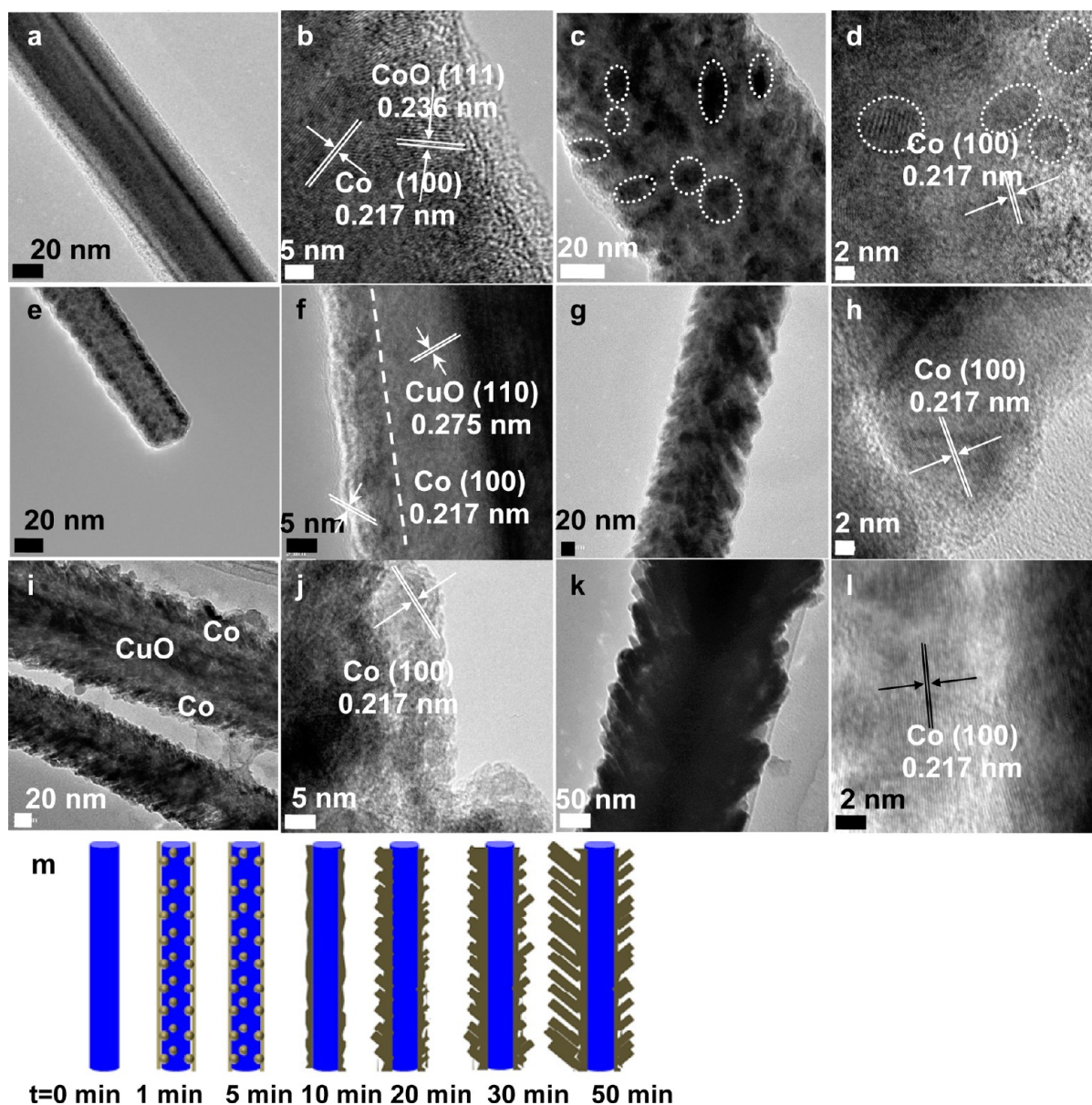
Figure 2. TEM images of CuO−Co nanowire heterostructures after sputter deposition of Co for (a,b) 1 min, (c,d) 5 min, (e,f) 10 min, (g,h) 20 min, (i,j) 30 min, and (k,l) 50 min and (m) schematic showing the morphological evolution of Co coating on CuO nanowires. Note: The dotted circles indicate the presence of Co nanoparticles embedded within Co thin film. The dotted line in (f) shows the interface between Co and CuO.

2.4. Absorbance and Band Gap Energy Measurements. The reflectance spectra for the samples (as-produced CuO nanowires, Co_3O_4 nanotubes, and CuO−Co_3O_4 nanowire heterostructures) used for photodegradation studies were obtained using reflectance mode UV−vis spectroscopy. Band gap energies were derived using Kubelka−Munk (α) function as follows:[38]

$$\alpha = (1 - R)^2/2R = K/S \qquad (2)$$

where R is the measured reflectance of the sample (ratio between R_{sample} and $R_{standard}$), K is the absorption coefficient, and S is the scattering coefficient. Assuming indirect band gap transition, $(\alpha h\nu)^{1/2}$ versus $h\nu$ was plotted, where where h is Planck's constant and ν is the frequency (s^{-1}). The intercept of the linear part of the plot on the x-axis (or $h\nu$ axis) indicates the band gap energy (eV).

3. RESULTS AND DISCUSSION

3.1. Fabrication of CuO−Co Nanowire Heterostructures and Their Growth Mechanism and Nanomechanics.

High aspect ratio and vertically aligned CuO nanowires (Figure S1a,1b) were grown by heating copper substrate in air with the growth governed by the vapor−solid (VS) growth mechanism.[35,39] The diameter, length, spatial density, and inter-nanowire spacing for the as-prepared CuO nanowires were ∼67.9 ± 18.6 nm, ∼5.0 ± 1.5 μm, ∼9.4 × 10^8 per cm^2, and ∼267 nm, respectively. Majority (∼90%) of as-produced CuO nanowires were observed to be at low tilting angles (<10°) on the substrate, and ∼10% of the observed nanowires were tilted at angles between 10 and 70° (Figure S1g). Subsequently, CuO nanowires were sputter-coated with Co (Figures S1c). In order to vary the thickness (or Co content), morphology, and crystallinity of the Co coating, the process of Co sputter deposition was studied as a function of deposition duration (Table S1, A series samples).[31] Standing CuO−Co nanowire heterostructures were observed at different Co sputtering durations (1 to 50 min, Figure 1a−f). There were
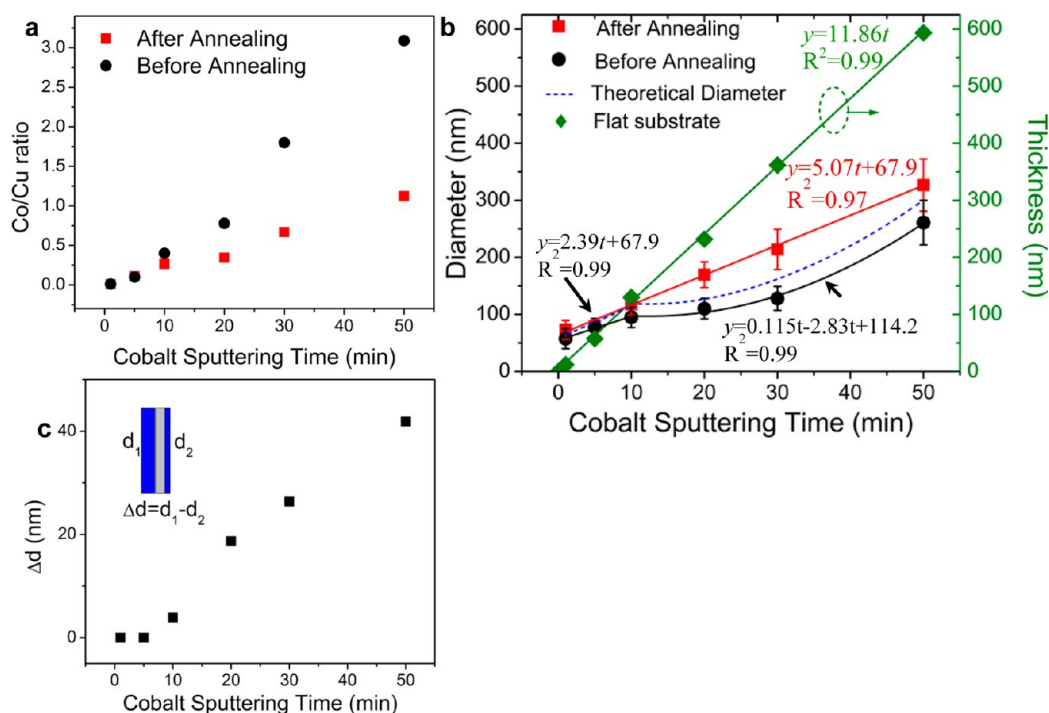
Figure 3. Plots showing (a) Co content, (b) nanowire heterostructure diameter, and (c) nanowire self-shadowing effects as a function of Co sputtering duration. Note: Co/Cu atomic ratio in (a) was estimated using EDS of CuO−Co nanowire heterostructures before and after air annealing. (c) Co shell thickness difference (shadowing effect, Δd, as shown in the schematic in the inset) between two sides of core CuO nanowires before and after air annealing as a function of Co sputtering duration. Linear fit (green color, control sample) in (b) shows the thickness of the Co film on a flat Si/SiO_2 substrate as a function of Co sputtering duration.

also some bent nanowires present at longer sputtering durations (>20 min, Figure S2). The bending angle of the nanowire (typically near the tip) increased from ∼12−39° for 20 min to ∼23−78° for 50 min (Figure S3). This bending could be attributed to the force (or rate of change of momentum) with which incident Co species impinged onto nanowire tips and nearby regions.[40] Co loading and the stiffness of nanowire with time were critical and are evaluated later in this article. The Co coating on CuO nanowires was dominantly amorphous with nanocrystalline domains of Co and its oxide (due to air exposure, Figure 2). This amorphous phase formation depends on the sputtering conditions and crystal structure difference between CuO and Co,[31] which resulted in anomalously fast diffusion and surface migration of the Co on the nanowire surface.[41] After a specific thickness of the amorphous Co deposited on the CuO nanowires, surface diffusion of the depositing Co species may be suitably slow to allow for the formation of crystalline Co domains in the coating (Figure 2).[41] The morphological evolution of the Co coating on CuO nanowires as a function of sputtering duration is schematically illustrated in Figure 2m. In the first 10 min, the Co coating in the form of a thin shell with embedded nanoparticles (∼7.6 ± 2.1 nm) evolved, which beyond 10 min resulted in "fir-tree"-like coating with columnar and semi-crystalline Co grains (Figures 2g−l). These columnar grains were inclined at an angle (45−50°) with respect to the CuO nanowire axis, and the former were also tilted opposite to the direction of the incident depositing Co in the sputtering process (Figures S4 and S5).

On the basis of SEM, TEM, and EDS analyses, it was possible to measure the Co content and diameter of the CuO−Co nanowire heterostructures as well as nanowire self-

shadowing effects, all of which increase/enhance with Co sputtering duration (Figure 3). According to quantitative estimation, the atomic ratio of Co to Cu on CuO nanowires (Figure 3a) increased with deposition time of 0.01 (for $t = 1$ min) to 1.124 ($t = 50$ min), indicating ∼112.4 times increase and also demonstrates an ability to control the Co content on the nanowires. Average diameter of the nanowires after Co coating showed an increasing trend ranging from ∼69.4 ± 17.6 nm at 1 min to ∼261.1 ± 39.2 nm at 50 min sputtering duration (Figure 3b, black color fit). Linear trend in the diameter was only observed until 10 min; beyond this, a quadratic polynomial fit was observed. The rate at which the diameter of the nanowires increases as a function of sputtering duration is governed by two fundamental mechanisms:[42,43] (1) Stranski−Krastanov (SK) near-equilibrium mode for the first 10 min of sputter deposition at a rate of ∼2.39 nm/min and (2) kinetic roughening of the nanowire surface at sputtering durations above 10 min, leading to low surface diffusion rates and growth of columnar Co coatings. As shown in Figure 2m, the presence of Co nanoparticles embedded within the Co thin film on CuO nanowires (<10 min) suggests that the SK mode was the dominant Co coating mechanism[42,44] and was assisted by significant surface diffusion of Co onto CuO nanowires. In the latter regime (10−50 min), a negligible initial growth rate (10 min < t < 20 min) indicates the merging of clusters and grain boundary formation.[41,42,45] As the growth rate increased (t > 20 min), columnar grains emerged, indicative of low surface diffusion rates and dominating kinetic effects based on deposition and surface transport rates.[42] The average width of columnar grains increased from ∼18 to ∼25 nm for 20 to 50 min sputter deposition. The voids between the columnar grains[46] grew smaller in size for longer sputtering duration (t =
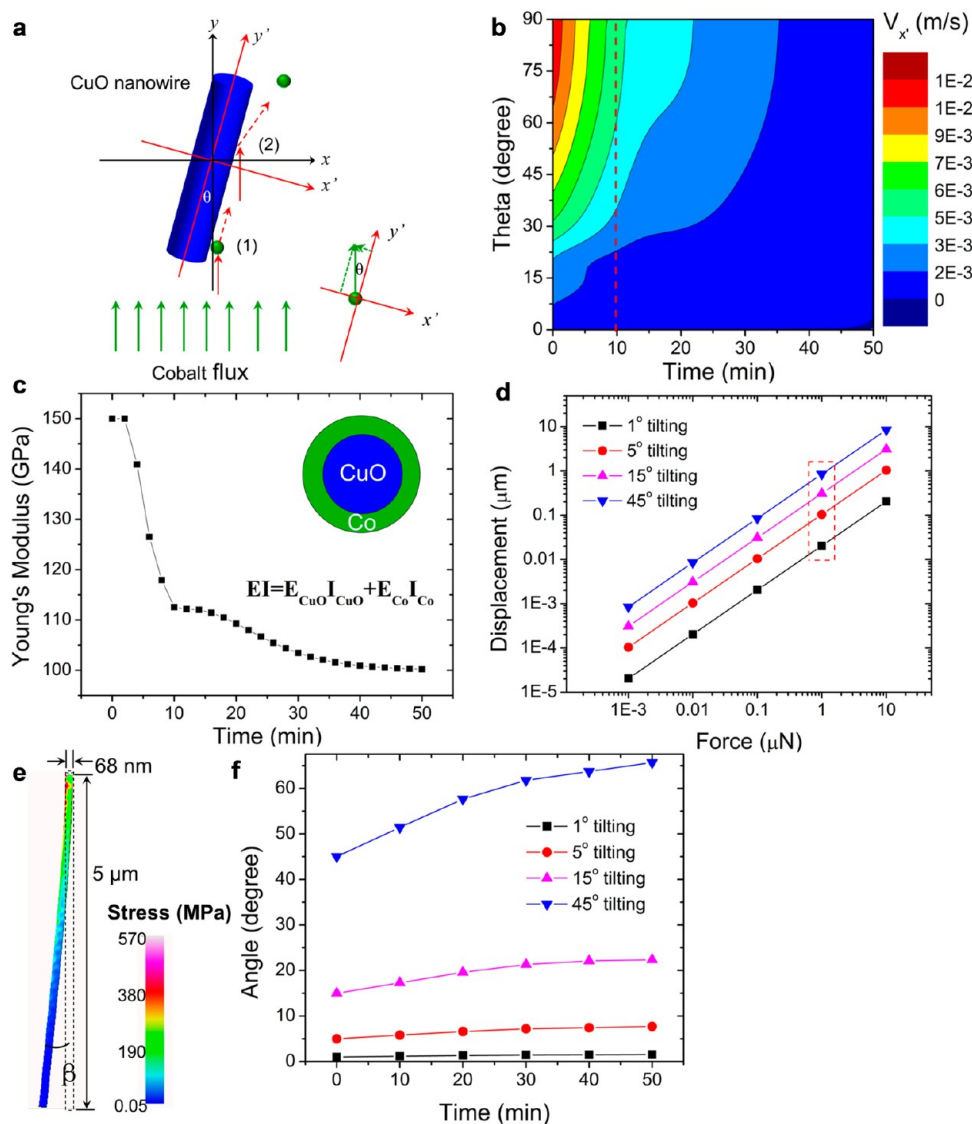
Figure 4. (a) Schematic illustrating Co species (green) impinging onto the CuO nanowire (blue) in the sputter deposition process. (b) Three-dimensional plot showing dependence of $V_{x'}$ with respect to Co sputtering duration and nanowire tilting angle (θ). (c) Young's modulus of CuO–Co nanowire heterostructures as a function of sputtering duration. (d) FEM analysis plot of displacement of pure CuO nanowire vs impinging force and the derived image showing (e) the bending and von Mises equivalent stress distribution in the nanowire. (f) FEM analysis plot for nanowire heterostructure swaying angle (bending) vs Co sputtering duration. Note: The force in (f) was assumed to be 1 μN, as shown by the dotted rectangle in (d).

50 min) as this involved kinetic roughening of surface and facilitated grain boundary grooving.[42]

The growth rates for Co coating around CuO nanowires were observed throughout to be significantly lower (~5 times) than that of the control sample (~11.85 nm/min, green color linear fit in Figure 3b), which was prepared by sputtering Co on a flat substrate (Si/SiO$_2$ surface). This flat film deposition process exhibited a linear deposition trend as a function of deposition duration, which confirms that the sputter deposition process on single-crystalline substrates with high curvature (nanowires) is drastically different than that on a flat substrate. Another important observation in the case of Co deposition on CuO nanowires was the shadowing effect due to the nanowires, which has been observed for other systems.[47] The shadowing effect was estimated based on the difference (Δd, Figure 3c and inset) of TEM-observed Co coating thickness on both sides of the nanowires. This Δd value increased from 0 to ~41.8 nm

within 5 to 50 min of Co sputtering. This indicates that the nanowire surface facing the incident material captured more Co, making surface migration the dominant mechanism responsible for the complete diametrical and longitudinal coverage (Figures 1 and 2).

In regard to the uniformity of Co coating around nanowires, a possible argument could be that the mean free path of the incident Co species (~2.57 cm, Supporting Information) was significantly (~9.63 × 10^4 times) greater than the spacing between CuO nanowires (~267 nm), the latter acting like a nanopore. Thus, Co species entering this nanopore likely encountered a large number of collisions with the adjacent nanowire surfaces mimicking a Knudsen diffusion process.[48] This reasoning should indicate that only the tips and the nearby regions of the nanowires would be coated with Co. However, our microscopic observations contradicted this and showed uniform coating of nanowires with Co along its length (Figures

1, 2, and S5). Thus, other factors such as chemical potential of the nanowires and Co surface migration on nanowires must play a role here.[5,49] A possible mechanism could be that as soon as the Co species impacts the nanowire, it gained significant momentum along the nanowire axis. In addition, the nanowire surface (curved) had a higher chemical potential than the base substrate (flat),[24] which enhanced surface migration and led to Co coating along the overall length of the nanowires.

To understand this, it is critical to evaluate the material surface migration on the nanowire surface. Thus, further theoretical analysis was conducted. Consider at time $t = t$, incident Co flux (or momentum vector, $P_{incident\ Co}$) was perpendicular to the Co target and had an angle of θ (nanowire tilting angle) with the longitudinal direction of the CuO nanowire (Figure 4a). The following assumptions were made: (1) The mass of the nanowire at $t = t$ was $m_{CuO/Co}$ and was a summation of mass of CuO nanowire and the deposited Co. (2) The mass of one unit of incident Co in the incoming flux (Φ = number of Co species per nanowire per second) was m_{Co}, and the sticking coefficient was α.[50] To simplify the calculations, the average value of α for Co species throughout the sputter deposition process was considered to be ~0.75.[51] (3) The incident Co flux was uniformly impinging on the nanowire surface and further divided into two components; the first component is due to the sticking coefficient (α), which accounted for the fraction of actual Co species being absorbed/deposited. These Co species would still have a velocity $V_{surface}$ (surface migration velocity, situation (1) in Figure 4a) along the nanowire longitudinal axis (y'). The second component is due to the desorbing Co species, which is assumed to undergo a purely elastic collision on nanowire at an incident angle θ, same as the nanowire tilting angle (pure reflection, situation (2) in Figure 4a). The fraction of these species corresponds to $1 - \alpha$ (reflecting coefficient). (4) The base of the CuO nanowire is assumed to be anchored on the substrate. Using flat film calibration data (green color linear fit in Figure 3b) and kinetic energy calculations (Supporting Information), the number of Co species per nanowire per second (Φ) was calculated to be ~7.14×10^4, and impinging velocity of the cobalt species (V_{Co}) was estimated to be ~156 m/s.

On the basis of all the above assumptions and calculations, the overall mass of Co species depositing on an individual CuO nanowire was $m_{Co}\alpha\Phi$ (g/s) and the momentum of incident Co species per CuO nanowire was $\alpha\Phi(2m_{Co}E_k)^{1/2}$. Thus, by conservation of momentum (Figure 4a), the following equation is obtained (bold letters denote vectors):

$$P_{incident\ Co} = P_{Co\ on\ CuO\ nanowire\ surface} + P_{Co\text{-}coated\ CuO\ nanowire}$$
$$+ P_{Co\ desorbed} \tag{3}$$

Balancing components (Supporting Information) on the x'-axis (nanowire transverse axis) and y'-axis (nanowire longitudinal axis) shown in Figure 4a resulted in nanowire velocity components ($V_{x'}$ and $V_{y'}$) as follows:

$$V_{x'} = \frac{(\alpha - 2)\Phi m_{Co} V_{Co} \sin\theta}{m_{CuO/Co} + \alpha\Phi m_{Co}} \tag{4}$$

$$V_{y'} = \frac{\alpha\Phi m_{Co} V_{Co} \cos\theta - \alpha\Phi m_{Co} V_{surface}}{m_{CuO/Co} + \alpha\Phi m_{Co}} \tag{5}$$

This momentum conservation approach explains two aspects: (a) displacement of nanowires like a hinged cantilever during the sputter deposition process, where $V_{x'}$ and $V_{y'}$ are the speeds at which this displacement takes place, and (b) migration of deposited Co species on the nanowire surface with velocity given by $V_{surface}$ on the x'-axis. Since we assume that the nanowire is anchored on the substrate, $V_{y'} \approx 0$ for a rigid nanowire (or nanowire is incompressible on the y'-axis). The following relationship using eq 5 can be derived:

$$V_{surface} = V_{Co} \cos\theta \tag{6}$$

Equation 6 indicates that, if the nanowire was vertically aligned, then the surface migration velocity ($V_{surface}$) was the highest ($\sim V_{Co}$). Thus, as soon as the Co species impinged on the surface of the nanowire (at $t = t$), the former displayed a tendency to surface migrate along the nanowire length. This also explains the uniform coating on the majority of the CuO nanowires because they were tilted by small angles ($\theta < 5°$, Figures S1g and S2) on the substrate. Thus, θ is a critical parameter determining the bending of nanowires and must be evaluated in detail. The authors propose that θ is also related to the nanowire motion (hinged cantilever-like bending or "swaying") in the x' direction due to the $V_{x'}$ velocity component (eq 4). Knowing that the nanowire diameter is a function of the sputtering duration (t, Figure 3b), it is possible to estimate $m_{CuO/Co}$ (Supporting Information). This further result in $V_{x'}$ as a function of both t and θ is shown in Figure 4b and given below (eqs 7 and 8):

For $0 < t < 10$ min (or 600 s)

$$V_{x'} = \frac{(\alpha - 2)\Phi m_{Co} V_{Co} \sin\theta}{3.49 \times 10^{-17}[(2.39t + 67.9)^2 - 1387] + \alpha\Phi m_{Co}} \tag{7}$$

For 10 min (or 600 s) $\leq t \leq 50$ min (or 3000 s)

$$V_{x'} = \frac{(\alpha - 2)\Phi m_{Co} V_{Co} \sin\theta}{3.49 \times 10^{-17}[(0.115t^2 - 2.83t + 114.2)^2 - 1387] + \alpha\Phi m_{Co}} \tag{8}$$

Figure 4b indicates that when θ is very high (>60°), the nanowire velocity ($V_{x'}$) was the highest (~1.0×10^{-2} m/s), and this velocity decreased with Co sputtering duration. This velocity ($V_{x'}$) was very low (between 0 and ~2×10^{-3} m/s) throughout the sputtering process for low θ (<10°). Thus, nanowire vertical alignment was the key in preventing nanowire bending and swaying (based on $V_{x'}$ dependence) as well as, in turn, minimizing the self-shadowing effects. In addition, higher $V_{x'}$ at larger θ implies that nanowires have a greater tendency to bend or sway. This could be the reason for observing large nanowire bending angles (Figures S2 and S3) and also suggests that the nanowires in our study were not 100% vertically aligned and some nanowires were at greater tilt angles ($\gg5°$) on the substrate (Figure S1g).

Assuming that the nanowire sways like a hinged cantilever during the sputtering process based on velocity, diameter, and mass estimations, it was possible to evaluate the stress distribution of the nanowires as a function of Co sputtering duration (t) and θ. The Young's modulus for pure CuO nanowires and Co coating as well as Possion's ratio for CuO nanowires were assumed as ~150 GPa, ~100 GPa, and ~0.3, respectively.[52,53] Thus, Young's modulus, based on effective flexural rigidity, of heterostructured nanowire is given as eq 9:[20,54]
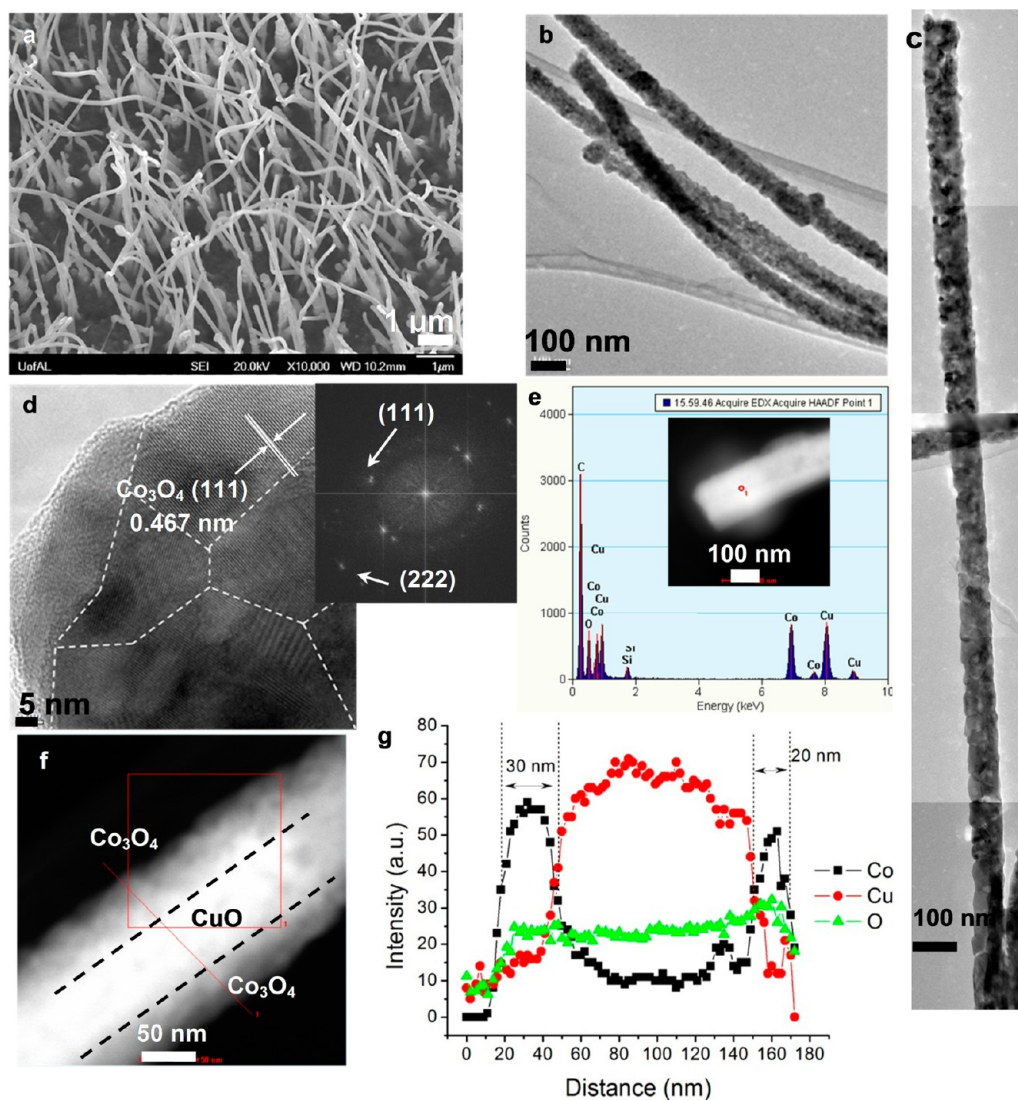
$$EI = E_{CuO}I_{CuO} + E_{Co}I_{Co} \tag{9}$$

Figure 5. (a) SEM image of standing CuO–Co$_3$O$_4$ nanowire heterostructures synthesized for conditions consistent with sample #3B. (b,c) TEM images showing CuO nanowires coated with Co$_3$O$_4$ after air-annealing process. (d) HRTEM image with dotted lines indicating grain boundary and FFT image for the Co$_3$O$_4$ coating. (e) Typical spot EDS analysis, (f) STEM mode image, and (g) EDS line profile of the CuO–Co$_3$O$_4$ nanowire heterostructures.

where E and I denote Young's modulus and moment of inertia of the individual component, respectively. The latter is given as $I_{CuO} = (d_{CuO})^4/12$ and $I_{Co} = [(d_{CuO/Co})^4 - (d_{CuO})^4]/12$, where d_{CuO} is ~68 nm and $d_{CuO/Co}$ is given as eq S4 in Supporting Information. Young's modulus of nanowire heterostructures versus t (Figure 4c) showed steep decline for the initial 10 min and showed a gradual decline beyond this duration with stabilization after 40 min. This implies that the Young's modulus of pure Co (~100 GPa) dominates the composite nanowire with thicker Co coating. This calculation is further utilized in finite element method (FEM) analysis as described next using ELMER software.[55]

The FEM mesh was created using GID 10.2 software with 0.15 mesh size. In order to evaluate nanomechanical aspects of CuO–Co nanowire heterostructures, the first step was to select suitable impinging force of the Co species during the sputtering process. FEM analysis resulted in a linear relationship between the impinging force and nanowire displacement or swaying (Figure 4d). This also showed that, at a constant force, higher θ resulted in larger nanowire displacements. Thus, selecting 1 μN

impinging force simplified subsequent calculations as higher forces would correspond to multiplying factors based on Figure 4d. This force value is also consistent with other nanowire systems.[40] A representative von Mises equivalent stress distribution in the pure CuO nanowire corresponding to 5° (=θ) nanowire tilt and 1 μN force is shown in Figure 4e. This force resulted in a nanowire swaying angle (β, Figure 4e and Figure S6a). The maximum von Mises equivalent stress distribution near the hinged location was calculated to be as high as ~400 MPa. The Young's modulus of CuO–Co nanowire heterostructures was obtained from Figure 4c. As the Co sputter deposition on CuO nanowires proceeded, FEM calculations (Figure 4f) indicated that this swaying angle (β) essentially remained the same throughout the sputtering process for small θ (<15°) but showed an increasing trend if the latter was greater than 15°. For example, a CuO nanowire tilted at 45° would be further swayed and bent by 65° after 50 min of sputtering duration. This bending is also responsible for the enhanced shadowing effects, confirming our observations (Figure 3c). At the same time, von Mises equivalent stress
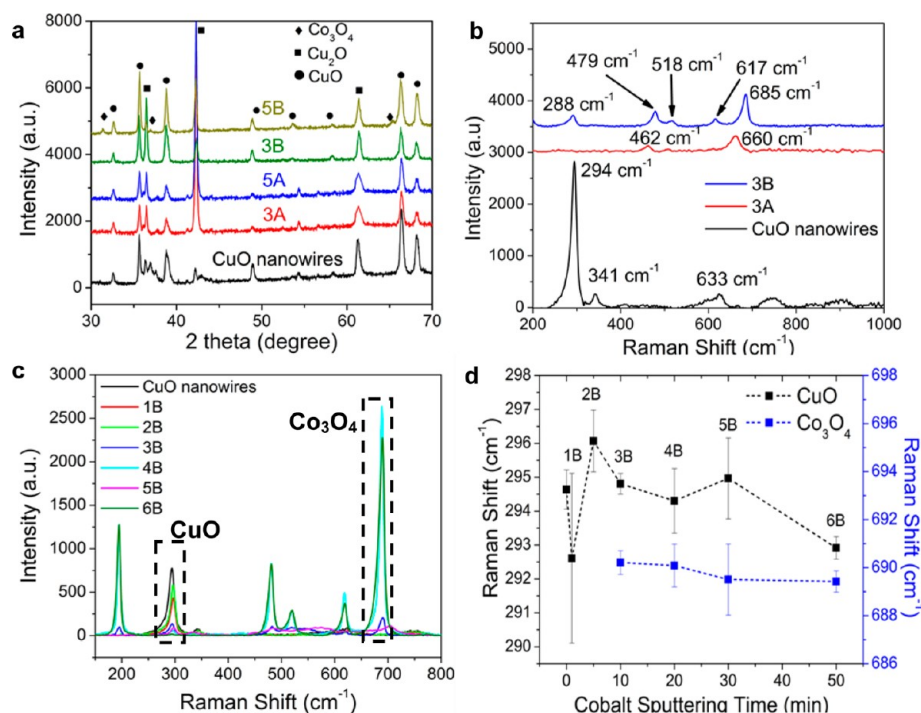
5597

dx.doi.org/10.1021/am301488c | ACS Appl. Mater. Interfaces 2012, 4, 5590–5607

Figure 6. (a) XRD patterns and (b) Raman spectra for CuO nanowires as well as CuO−Co and CuO−Co$_3$O$_4$ nanowire heterostructures (samples #3 and #5, Table S1). (c) Comparison of Raman spectra and (d) Raman peak locations for CuO (~294 cm^{-1}, dotted box in (c)) and Co$_3$O$_4$ (~700 cm^{-1}, dotted box in (c)) for various CuO−Co$_3$O$_4$ nanowire heterostructures (samples #1B−6B, Table S1) corresponding to different Co sputtering durations.

distribution intensified in the heterostructured nanowires with increasing sputtering duration and θ (Figure S6). It is estimated that the stress was concentrated at the root of nanowires,[56] which might cause the failure/breaking of nanowires if the impinging force or θ is large enough and Co sputtering duration is low (thin Co coating, Figure S6b). However, it must be noted that the maximum von Mises equivalent stress was calculated to be as high as ~200 MPa (for $\theta = 45°$ and $t = 50$ min), which is 2 times lower than that of the pure CuO nanowire. This is also obvious as the CuO−Co nanowire heterostructures have lower Young's modulus (lower stiffness) as compared to pure CuO nanowires (Figure 4c). Assuming that the plastic yielding stress for the nanowires is in gigapascal range,[53] this stress distribution (Figure S6b) suggests that CuO−Co nanowire heterostructures will be difficult to yield as compared to pure CuO nanowires. Our microscopic observations also showed negligible number of fractured nanowires and, thus, strengthen this argument. Overall, these calculations and theoretical approach clearly show that perfect vertical alignment ($\theta = 0$) in CuO nanowires is critical for minimizing the yielding and bending of nanowires as well as shadowing effects (Figures 4 and Figure S6) during the Co sputtering process. This will further allow for fabrication of stable CuO−Co nanowire heterostructures.

3.2. Fabrication of CuO−Co$_3$O$_4$ Nanowire Heterostructures and Their Morphological and Structural Evolution. The above-mentioned theoretical and experimental understanding for CuO−Co nanowire heterostructures is critical[57] for a uniform, mechanically stable, and controlled CuO−Co$_3$O$_4$ nanowire heterostructure formation after an air-annealing process (Table S1, sample series B). Due to the relatively higher melting points of Co and CuO compared to the annealing temperature, no physical damage, fusion, and

melting was observed.[58] As seen in the representative sample (sample #3B, Table S1, Figure 5a−d), nanowires were completely coated with a polycrystalline Co$_3$O$_4$ shell (lattice spacing in Figure 5b−d). Several STEM-mode EDS analysis and line profiles showed that both CuO and Co$_3$O$_4$ components were structurally and chemically intact within the nanowire heterostructures (Figure 5e−g). The shadowing effects with one side of the CuO nanowire showing higher Co$_3$O$_4$ shell thickness than the other ($\Delta d \sim 10$ nm) were also identified using line profiles and followed a similar trend as non-annealed samples (Figure 3c). XRD (Figure 6a) showed the phase and crystallinity of Co$_3$O$_4$ after the air-annealing process. Due to partially crystallized or amorphous Co coating and limitations in XRD resolution, it was not possible to observe Co in non-annealed samples (Figure 6a). Postannealing XRD for the nanowire heterostructures showed (Figure 6a) several new peaks at 31.11, 36.59, and 65.17° corresponding to (200), (311), and (400) planes of Co$_3$O$_4$, respectively (JCPDS 65-3103). Raman spectra confirmed the phases present in the nanowires at various stages of processing (Figure 6b). In Figure 6a,b, peaks at 294, 341, and 633 cm^{-1} could be ascribed to A$_g$, B$_g^1$, and B$_g^2$ modes of CuO nanowires, respectively.[59] After coating with Co, new Raman peaks corresponding to the oxides of Co (due to air exposure) emerged, consistent with the TEM observations (Figure 2). After air annealing, Raman peaks consistent with Co$_3$O$_4$ were observed at 288 cm^{-1} (F$_{2g}$), 479 cm^{-1} (E$_g$), 518 cm^{-1} (F$_{2g}$), 617 cm^{-1}(F$_{2g}$), and 685 cm^{-1}(A$_{1g}$).[60] The absence of a peak centered around 600 cm^{-1} can also confirm the good crystallization of Co$_3$O$_4$ within the heterostructure.[60] Compared with the standard spectra, the Raman peaks were slightly shifted (~1−3 cm^{-1}) and could be attributed to the nanostructured morphology, lattice strains, presence of heterojunctions, and/or sample variability (Figure
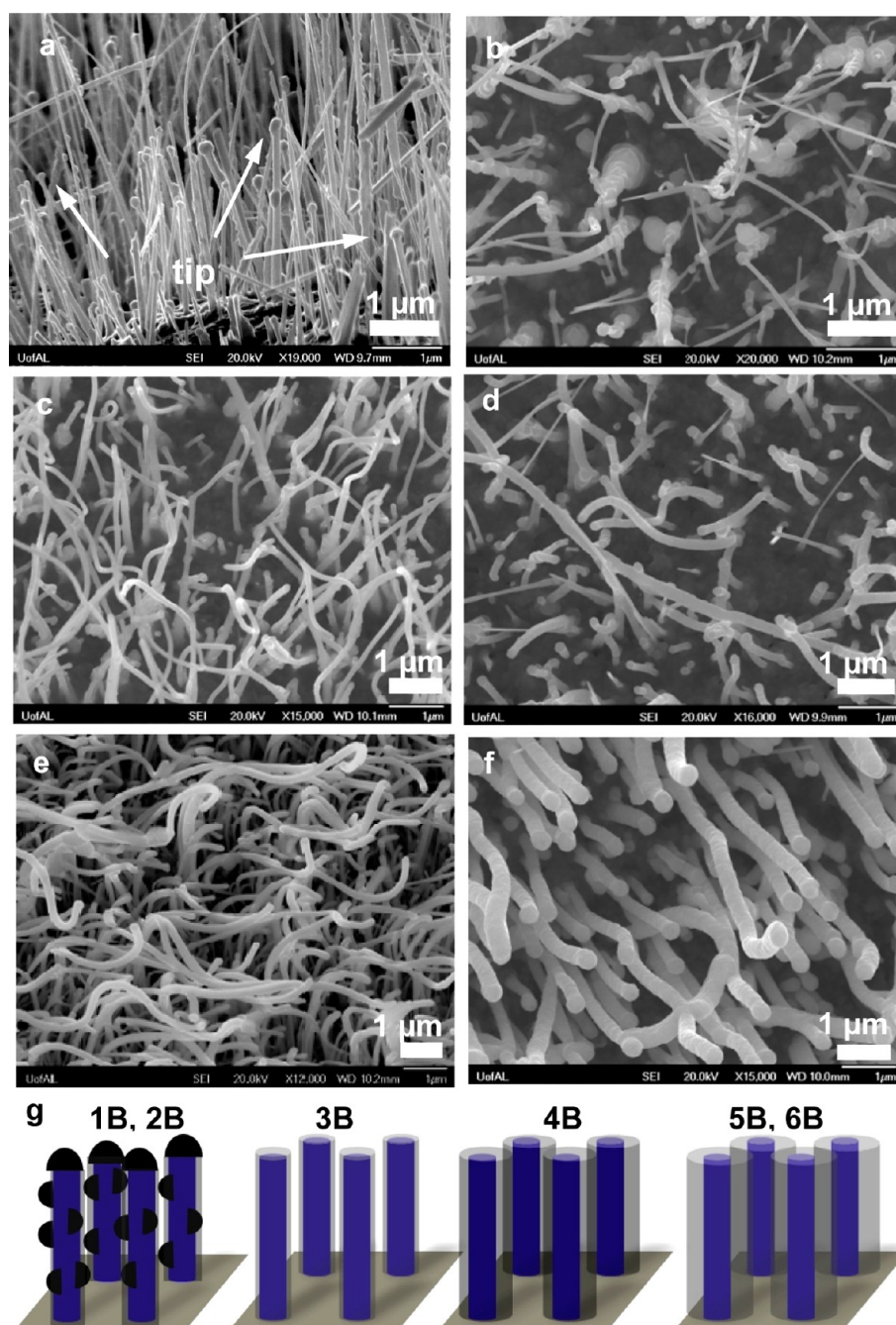
Figure 7. SEM images of standing CuO−Co$_3$O$_4$ nanowire heterostructures fabricated after air annealing (for 10 h) and corresponding to Co sputter deposition for (a) 1 min, (b) 5 min, (c) 10 min, (d) 20 min, (e) 30 min, and (f) 50 min sputtering (scale bar: 1 μm). (g) Schematic illustrating morphogical evluotion of Co$_3$O$_4$ on core CuO nanowires after annealing.

6c,d).[61] Raman depth profile (Figure S7a) on CuO−Co$_3$O$_4$ nanowire heterostructures showed Co$_3$O$_4$ peaks along the entire length of the nanowires (Figure S7a). A minor peak shift (∼1.1 cm^{-1}, Figure S7b) corresponding to the strongest Co$_3$O$_4$ (A$_{1g}$) Raman peak could be due to the stresses in the polycrystalline Co$_3$O$_4$ shell along the nanowire length.[61] Raman peak intensity was lowered by ∼250 units (Figure S7c) along the length of the nanowire. This lowering in peak intensity could be due to a sample-induced spherical aberration.[62]

The annealing of CuO−Co nanowire heterostructures corresponding to different sputtering duration (samples #1B−6B, Table S1, Figure 7) resulted in standing CuO−Co$_3$O$_4$ nanowire heterostructures with controlled Co content. Figure

7g shows the morphological evolution of Co$_3$O$_4$ on CuO nanowires. Samples #1B and #2B (Table S1), consistent with shortest Co sputtering duration of 1 and 5 min, respectively, resulted in Co$_3$O$_4$ nanoparticle formation within a thin film of Co$_3$O$_4$ (<1−2 nm). Interestingly, sample #1B showed Co$_3$O$_4$ nanoparticle decoration at the nanowire tip, indicating that surface migration during annealing drove the material toward low chemical potential regions of the nanowires (flat tips).[24] The nanowire heterostructure diameters versus Co sputtering duration after air-annealing process showed a linear trend (Figure 3b, red color fit). Theoretical estimation of this diameter, assuming that all of the Co on the nanowires completely converted into the Co$_3$O$_4$ shell (Figure S8),
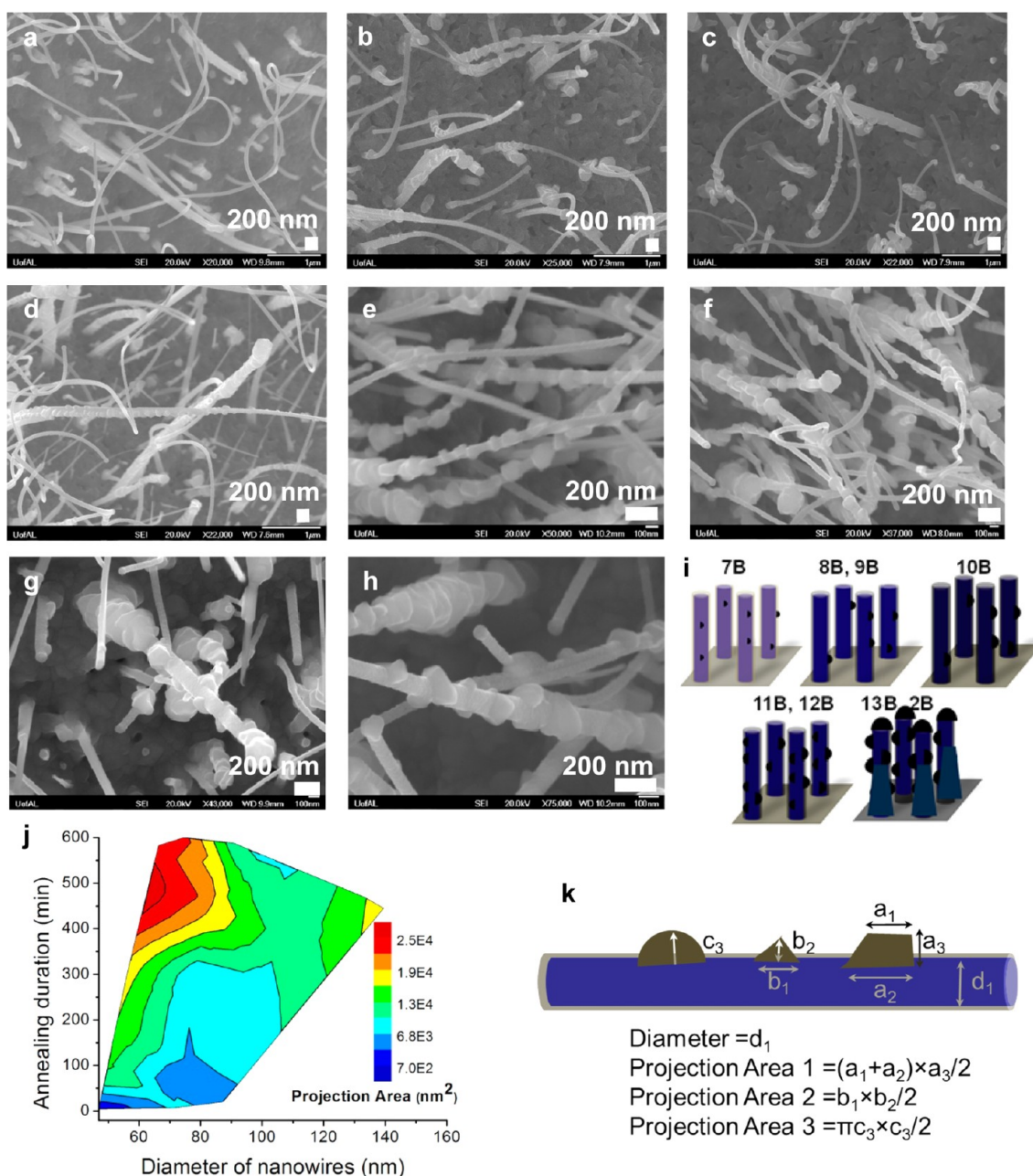
5599

dx.doi.org/10.1021/am301488c | ACS Appl. Mater. Interfaces 2012, 4, 5590−5607

Figure 8. SEM images of standing CuO−Co$_3$O$_4$ nanowire heterostructures after air annealing of CuO−Co nanowire heterostructures (samples #2A and #7A−13A, Table S1) for (a) 5 min, (b) 10 min, (c) 20 min, (d) 60 min, (e) 2.5 h, (f) 5 h, (g) 7.5 h, and (h) 10 h (scale bar: 200 nm). (i) Schematic representing morphological evolution of Co$_3$O$_4$ on core CuO nanowires as a function of air-annealing duration. (j) Contour plot showing Co$_3$O$_4$ nanoparticle projection area as a function of annealing time and diameter of nanowire heterostructures. (k) Schematic illustrating the approach to calculate nanoparticles' projection area.

resulted in a trend (Figure 3b, blue dotted line) similar to before annealing. So, the experimental observation of the linear trend for CuO−Co$_3$O$_4$ nanowire heterostructure diameter with a rate ∼2 times faster as compared to the theoretically calculated diameter suggests that the surface diffusion of the material was aided by the incorporation of extra Co content. The contribution of the latter must be attributed to the Co present at the roots of the nanowires (or on the substrate). It has been previously reported that the chemical potential effects of the nanowire surface as well as surface tension and surface charge of Co$_3$O$_4$ at the annealing temperatures play a dominant role. Furthermore, they also aid in migration of the material from the flat substrate to the nanowire surface when annealed

for longer durations.[5,24,31] It was observed that Co to Cu ratio (estimated using EDS, Figure 3a) for CuO−Co$_3$O$_4$ nanowire heterostructures increased with Co content (sputtering duration) but was lower than non-annealed samples due to the oxidation of Co.

Figure 8a−h shows CuO−Co$_3$O$_4$ nanowire heterostructures after air annealing for different durations (samples #2B and #7B−13B, Table S1). The Co sputtering duration for these experiments was fixed at 5 min as these conditions resulted in a thin film of Co with embedded nanoparticles of the same on CuO nanowires. Thus, the effect of the annealing duration on these samples was critical in understanding the interface development and morphological evolution of Co$_3$O$_4$ on the
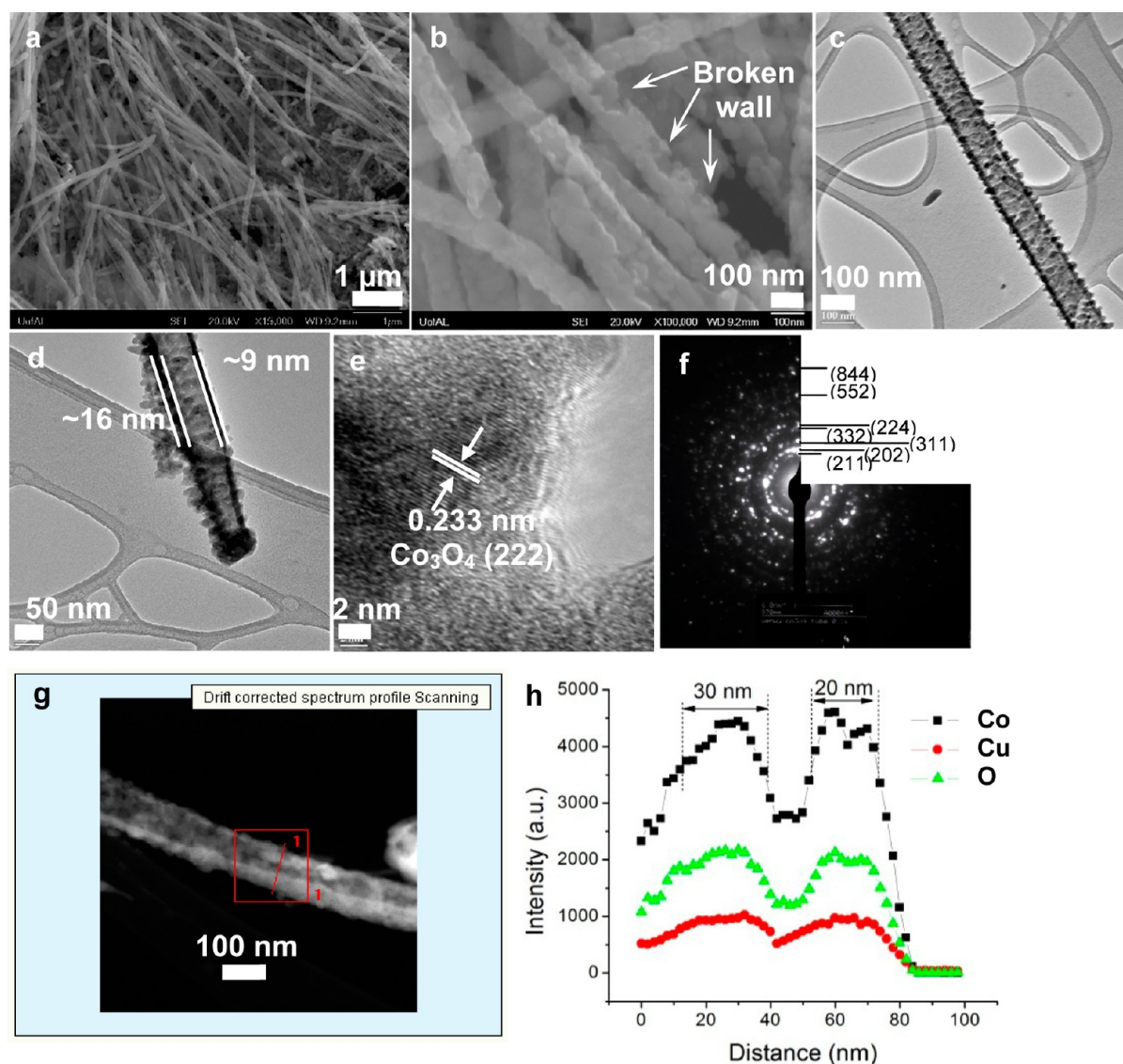
Figure 9. (a,b) SEM, (c−e) TEM images, (f) electron diffraction of Co_3O_4 nanotubes after selective etching of CuO nanowire cores, and (g) HAADF-STEM image of Co_3O_4 nanotubes and corresponding (h) EDS line profile. Note: The red line in (g) indicates the line profile scan path, and the rectangular box indicates the drift correction. Co_3O_4 nanotubes were fabricated by selectively etching CuO nanowires from sample #3B (Table S1).

CuO nanowires.[31] As the annealing duration was increased (5 min to 10 h), Co_3O_4 evolved on CuO nanowires in the form of polycrystalline film coating with several faceted nanoparticles (Figures 8i and S8). Annealing duration was plotted as a function of diameter of the nanowire heterostructures and the projection area of Co_3O_4 nanoparticles (Figure 8j and Table S2). The latter implies a 2-D projection, which is a better indicator of size and shape of the nanoparticle (Figure 8k). The average nanowire diameter was estimated only for those regions of nanowires that did not have any faceted nanoparticle growth and is observed to be constant, irrespective of the annealing duration (Table S3). The estimated projection areas of the nanoparticles formed were lower at smaller annealing durations (<2 h) than longer durations (Figure 8j). Only nanowires with diameters less than ~90 nm incorporated the largest possible sizes (or projection areas) of the nanoparticles. The nanowires with diameters greater than ~90 nm resulted in more uniform nanoparticle sizes after annealing. Furthermore, the nanoparticle size tended to stabilize at moderate annealing

conditions and with larger diameters of nanowires. The formation of larger-sized faceted nanoparticles was also enhanced in longer annealing durations (6−10 h), and under these conditions, smaller nanowire diameters (<73 nm) were observed (Table S3).

Several factors must be responsible for the morphological evolution of Co_3O_4 on CuO nanowires in this study. These competing mechanisms include Ostwald's ripening, thermodynamic imbalance, surface tension, surface charge, and stresses in the evolving Co_3O_4 morphologies. All of these could explain the larger size and faceting of the nanoparticles with increasing annealing durations. In addition, the self-diffusion of Co (order of 10^{-5} cm^2/s) and Co_3O_4 (order of 10^{-12} cm^2/s) was negligibly small[31,63] at the annealing temperatures in this study, and thus, the above-mentioned competing mechanisms become more critical to consider. In regard to thermodynamic imbalance, solid aggregate vapor pressure of Co_3O_4 around each nanowire must increase with annealing duration, which resulted in nonzero Gibb's free energy (ΔG), necessitated

change in surface energy of Co_3O_4, and led to the faceted growth of Co_3O_4 nanoparticles.[24] The particle size further increased with the annealing durations due to the intensified Ostwald's ripening effect. With all of these combined with chemical potential gradient,[24] the process facilitated material migration from nanowires (high curvature) toward the base (low curvature) or flat nanowire tips and resulted in tapered shape and material accumulation at the nanowire tip (bulb-shaped morphology, Figure 8h). This caused the slight decrease in diameters of nanowires for longer annealing durations. The chemical potential gradient accounts for the stress on the oxidizing Co film,[5] affecting the morphological evolution of Co_3O_4 on CuO nanowires. On the other hand, the surface charge of Co_3O_4 is strongly dependent on the surface energy and oxygen content in the annealing environment.[24] With increasing annealing duration, greater Co_3O_4 content and faceted nanoparticles are formed in these nanowire hetero-structures, which implies greater electrostatic repulsion for the Co_3O_4 grains due to surface charging. Finally, lattice compatibility at the interface of CuO and Co_3O_4 cannot be ruled out.[24,64]

In regard to interfaces, CuO−Co_3O_4 nanowire hetero-structures that were prepared after short air-annealing durations (<10 min) were analyzed (Figure S10). A good lattice match between the CuO and Co_3O_4 was observed at the interface. The lattice of monoclinic CuO nanowires with (200) planes matched well with the lattice of (111) planes of spinel Co_3O_4 (Figure S7c,g).[24] Moreover, for planes other than these, a certain extent of lattice mismatch or distortion was observed at the interface (Figure S7d). This is further confirmed by the FFT image (Figure S7e,f), where the dotted lines connecting diametrically opposite indices correspond to CuO (white) and Co_3O_4 (red). It has been observed earlier that, as soon as a good lattice match is established during the annealing process, the surface migration of Co_3O_4 on CuO nanowires is severely limited and could be the reason for uniform Co_3O_4 coating in our study.[24]

To demonstrate that the nanowires were coated uniformly with Co_3O_4 and this shell is polycrystalline, the core CuO nanowires (using sample #3B, Table S1) were selectively etched in a dilute acid. This resulted in polycrystalline nanotubes of Co_3O_4 (Figure 9). However, several of these nanotubes were broken (grain detachment) at multiple locations along the length (arrows in Figure 9b). This could be due to the nonspecific etching, imperfect packing of the coated Co_3O_4 shell, and high centrifuge speed (~6000 rpm) during the cleaning process. The average diameter of the Co_3O_4 nanotubes (~113.5 ± 23.3 nm) was not significantly different from that of the CuO−Co_3O_4 nanowire heterostructures (~117.8 ± 19.3 nm, sample #3B, Table S1). This confirms that there were negligible stresses within the Co_3O_4 coating on the CuO nanowires because, otherwise, after the selective removal of core CuO nanowires, Co_3O_4 nanotubes would have had a significant diameter reduction or structural collapse. The majority of nanotubes remained anchored to the base substrate but bundled near the tip region due to capillary action and drying of the etchant solution (Figure S11). The shadowing effect by virtue of line-of-sight Co sputter deposition could be clearly seen in the Co_3O_4 nanotubes, where the shell thickness difference between ~5 and 7 nm was observed (Figure 9d). Various crystal planes were observed (Figure 9e,f) for polycrystalline nanotubes with none corresponding to CuO. However, high-angle dark-field scanning transmission electron

microscopy (HADDF-STEM) mode EDS line profiles (0.1 nm probe size) showed minor copper signal indicating that there was negligible CuO left at the inner walls of the nanotubes (Figure 9g,h). Pure and polycrystalline Co_3O_4 nanotubes would be obtained if the etching process and conditions were precisely controlled and is a subject of further study in the authors' laboratory.

3.3. Band Gap Energy and Phenol Photodegradation Studies Using CuO−Co_3O_4 Nanowire Heterostructures as Photocatalysts. We evaluated the effects of morphology of CuO−Co_3O_4 nanowire heterostructures (samples #1B−6B, Table S1) on their UV absorption characteristics and band gap energies. Multiple absorption edges for the as-produced CuO nanowires[24] and CuO−Co_3O_4 nanowire heterostructures were observed (Figure S12a). Considering them as indirect band gap semiconductors, we converted the spectra into Tauc plots (Figure S12b−h),[24,38] where intercepts of the extrapolated linear region(s) on the x-axis correspond to the band gap energy. The band gap tailing was observed due to the morphology and quantum confinement effects.[6,24] The as-produced CuO nanowires exhibited a band gap of ~1.6 eV with a tailing of ~1.25 eV. However, careful analysis of absorbance of CuO nanowires also showed edges centered on ~280, ~390, and ~500 nm (Figure S12a).[24] The former two edges were attributed to the presence of CuO and Cu_2O thin films, which emerged by virtue of the VS growth mechanism for CuO nanowires.[35,39]

Nanowire heterostructures exhibited band gap energies ranging from 1.1 to 3.0 eV (Figure S12b−g),[24,65] whereas bulk CuO and Co_3O_4 systems have band gap energies of ~1.5 and 2.0 eV, respectively, without any band gap tailing.[66] Absorbance versus wavelength plots showed the development of new absorption edges in UV and visible range for each of the nanowire heterostructure samples (Figure S12a). Among all of the samples, strongest edges emerged in samples #4B and #2B, with Co_3O_4 as a thick polycrystalline shell (Figure 7d, shell thickness ~50.8 nm in Table S4) in the former and nanoparticles embedded in thin film (shell thickness ~5.6 nm in Table S4) in the latter (Figures 7b and 8h). The average size of the embedded nanoparticles was observed to be ~154.7 ± 16.9 nm. Interestingly, sample #2B exhibited more discrete band gap tailing (Figure S12c,d) as compared to polycrystalline shell morphologies (Figure S12d−h). The former could also be attributed to interfacial charge transfer processes associated with O^{2-} to Co^{2+} or Co^{3+} transitions coupled with core CuO nanowires.[24,67] Band gap energy of the nanoparticles is inversely proportional to their size.[68] For example, ~5.7 and ~47 nm diameter Co_3O_4 nanoparticles exhibited band gap energy of ~1.82 and 1.38 eV, respectively.[69] In addition, it has been demonstrated earlier that incorporation of Co_3O_4 nanoparticles on other inorganic nanoparticles and nanowires resulted in increases in their light absorption due to the narrow band gap of Co_3O_4 nanoparticles.[24,70] These arguments clearly support and explain discrete and narrow band gap energy and tailings observed for sample #2B (Figure S12d) having CuO nanowires coated with Co_3O_4 thin shell and embedded nanoparticles. On the other hand, in the case of thicker and polycrystalline Co_3O_4 shells, the Co_3O_4 grain size was most optimized for sample #4B and resulted in narrow band gap energy and tailings (Figure S12f). However, broadening of band gap energies was observed for samples #5B and #6B, which had very thick (>70 nm) and polycrystalline Co_3O_4 shells. These shells could also be considered as comprising
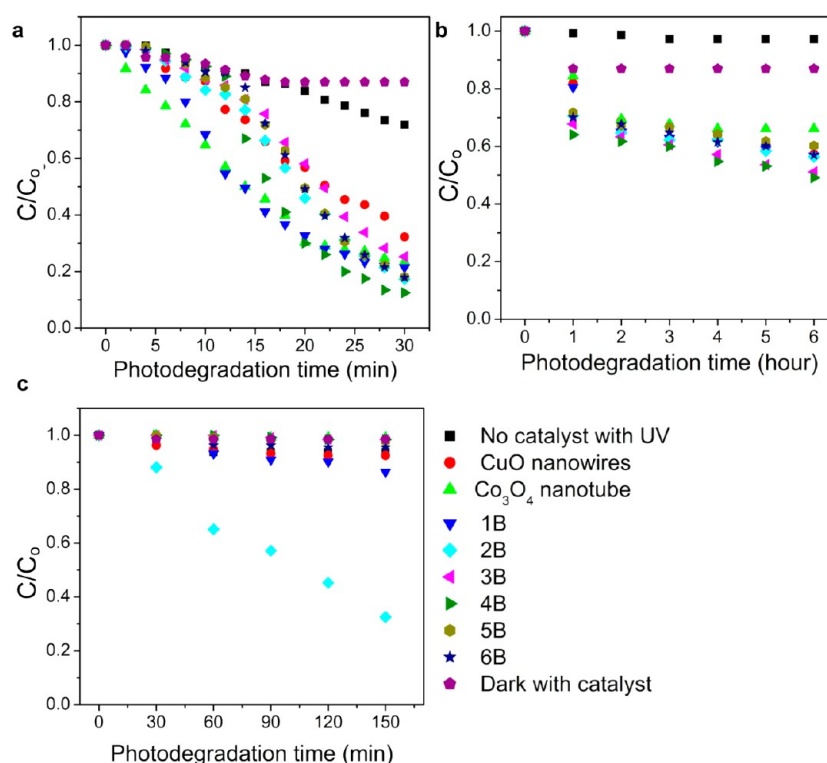
5602

dx.doi.org/10.1021/am301488c | ACS Appl. Mater. Interfaces 2012, 4, 5590−5607

Figure 10. Phenol photodegradation (conversion ratio) using CuO−Co$_3$O$_4$ nanowire heterostructures (samples #1B−6B, Table S1) as a function of reaction time under (a) UV illumination ($\lambda \sim$254 nm) and a sacrificial agent (H$_2$O$_2$), (b) visible light illumination ($\lambda \sim$580 nm) and H$_2$O$_2$, and (c) visible light illumination ($\lambda \sim$580 nm) and without H$_2$O$_2$.

aggregated or coalesced particles[69,70] of Co$_3$O$_4$ and the reason for the band gap broadening and greater extent of band gap tailing. Overall, the shift of absorption edges (Figure S12a) as compared to bulk Co$_3$O$_4$ edges was observed due to heterostructuring and nanostructuring of the CuO and Co$_3$O$_4$ system, morphology of Co$_3$O$_4$, and interfacial relationships between the core nanowire and the coated Co$_3$O$_4$.[24,70] It is anticipated that these nanowire heterostructures will be multiwavelength photoactive from UV to visible range.

Phenol photodegradation in water using UV and visible light was conducted for the nanowire heterostructures (samples #1B−6B, Table S1), as-produced CuO nanowires, and Co$_3$O$_4$ nanotubes (Figure 10). The characteristic UV absorption peak for phenol is shown in Figure S13. The experiments were divided into three different sets based on illumination and degradation conditions: (1) under UV light ($\lambda \sim$254 nm) with sacrificial agent (H$_2$O$_2$), (2) under visible light ($\lambda \sim$580 nm) with H$_2$O$_2$, and (3) under visible light ($\lambda \sim$580 nm) without H$_2$O$_2$. Four kinds of control experiments for photodegradation of phenol were performed: (a) with catalyst (CuO nanowires) in the dark and with or without H$_2$O$_2$, (b) without any catalyst in UV light and with H$_2$O$_2$, (c) without any catalyst in visible light and with or without H$_2$O$_2$, and (d) with Co$_3$O$_4$ nanotubes under UV or visible light and with or without H$_2$O$_2$. Highest photodegradation efficiencies (η) were observed for UV illumination and in the presence of H$_2$O$_2$ (Figure 11 and Table S4). The photodegradation was observed to be rapid in the case of UV illumination with H$_2$O$_2$ (Figure 10a) and slowest in visible light illumination with or without H$_2$O$_2$ (Figure 10b,c). This is also consistent with the absorbance behavior of the samples, which showed greater activity in the UV region than in the visible region. Under UV illumination, phenol degradation without catalyst but with H$_2$O$_2$ was $\sim$10

times higher ($\eta \sim$28.1%) than in the case of visible light with or without H$_2$O$_2$ (Table S4). Without illumination and using CuO nanowires as catalysts, η was $\sim$13% in the presence of H$_2$O$_2$ and was $\sim$1.5% in the absence of H$_2$O$_2$, which indicates that phenol can self-degrade in the dark with the aid of H$_2$O$_2$. Using CuO nanowires as photocatalysts, it was possible to obtain η $\sim$67.6, $\sim$42.8, and $\sim$8.9% with UV illumination and H$_2$O$_2$, visible illumination and H$_2$O$_2$, and visible illumination without H$_2$O$_2$, respectively. In regard to Co$_3$O$_4$ nanotubes, these efficiencies (Table S4) were increased (76.6%) in the case of UV illumination with H$_2$O$_2$ degradation but decreased ($\sim$33.9%) for visible illumination with H$_2$O$_2$, and further to $\sim$2.2% for visible illumination without H$_2$O$_2$. Thus, Co$_3$O$_4$ alone has low photodegradation ability in visible light and necessitates a sacrificial agent to achieve higher η.

CuO−Co$_3$O$_4$ nanowire heterostructures showed improved η as compared to control samples (Figure 10a−c). Table S4 shows the Co$_3$O$_4$ shell thickness corresponding to various nanowire heterostructure samples. For UV illumination with H$_2$O$_2$, η was greater than $\sim$75% for all of the samples during 30 min of degradation reaction, implying that the heterostructures' photodegradation performance is better under these conditions. Sample #4B showed highest η ($\sim$87%) for UV illumination with H$_2$O$_2$, and this trend was followed ($\eta \sim$50.8%) in visible illumination with H$_2$O$_2$. Notably, visible illumination without H$_2$O$_2$ showed anomalous photodegradation behavior for sample #2B ($\eta \sim$69.6%) as compared to the other samples, where η never surpassed $\sim$14% (Table S4). Sample #4B showed significantly low η ($\sim$1.6%) without H$_2$O$_2$, which indicated a strong dependence of the performance on the presence of H$_2$O$_2$. The dependence of η on the Co content is shown in Figure 11a, which also suggests that controlled nanowire heterostructure morphology can result in a simple
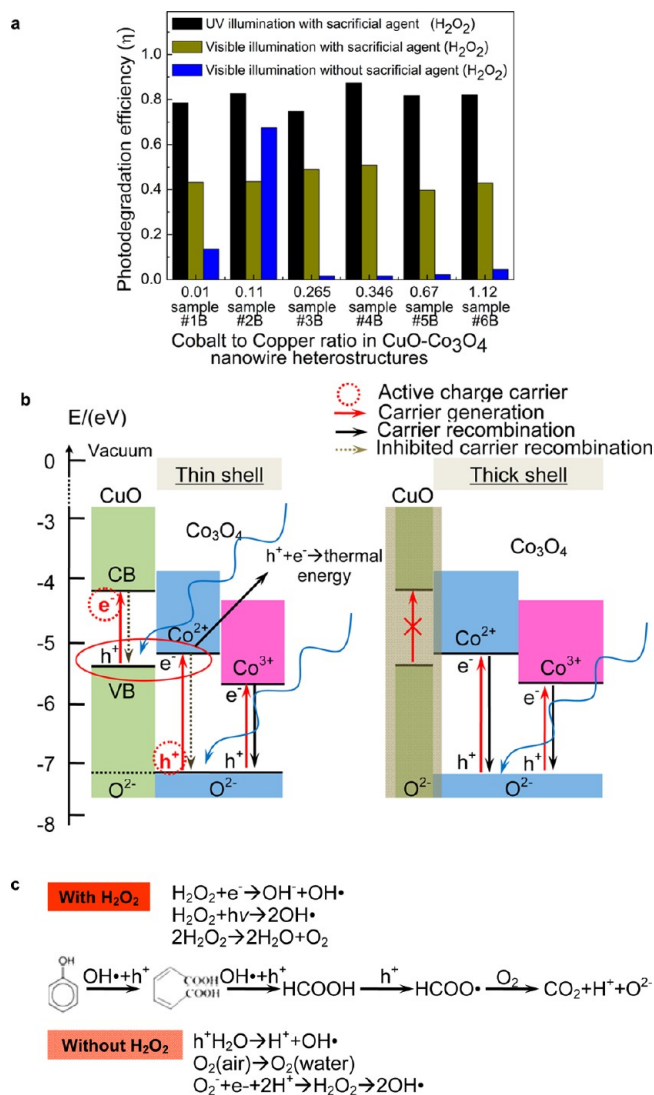
Figure 11. (a) Comparison of phenol photodegradation efficiency (η) for different samples and reaction conditions, (b) schematic illustration of band gap energies of CuO−Co$_3$O$_4$ nanowire heterostructures and the proposed charge transfer or separation mechanism, and (c) possible chemical reactions for photodegradation with and without H$_2$O$_2$. Note: The schematic in (c) on the left corresponds to sample #2B and on the right is consistent with sample #4B.

and noncontaminated photodegradation scheme that could completely eliminate the need for a sacrificial agent. A previous report on Co$_3$O$_4$ nanoparticle-coated BiVO$_4$ particles evaluated the role of Co content.[70] It was observed that the high Co content resulted in aggregated Co$_3$O$_4$ nanoparticles after the calcination process, which significantly lowered the photocatalytic activity of the composite nanopowders.[70] This argument is relevant to the CuO−Co$_3$O$_4$ nanowire heterostructures with thicker Co$_3$O$_4$ shells (samples #4B, #5B, and #6B) in our study. This combined with our explanation of the broadening of band gaps (Figure S12g,h) explains why these samples showed high activity only under UV illumination and in the presence of sacrificial agent (H$_2$O$_2$).

Consistent with our band gap energy results based on the Tauc plots (Figure S12), it could be clearly observed that nanowire heterostructures (samples #2B and #4B) with narrow band gap energies and tailings resulted in best photo-

degradation performance. A thick polycrystalline shell of Co$_3$O$_4$ on CuO nanowires (e.g., sample #4B, critical shell thickness ∼50.8 nm) made the latter optically opaque to incident light and resulted in charge transfer processes dominated by Co$_3$O$_4$. The visible light may not provide enough energy for suppressing the charge recombination and scattering due to Co$_3$O$_4$ shell thickness/polycrystallinity and could be the reason for the need of a sacrificial agent (H$_2$O$_2$) to achieve higher η for sample #4B. On the other hand, when the Co$_3$O$_4$ shell was very thin (e.g., sample #2B, critical shell thickness ∼5.6 nm) with nanoparticles embedded within, the following are proposed: (1) core CuO nanowires were also photoactive along with the Co$_3$O$_4$ shell; (2) the narrow band gap due to embedded Co$_3$O$_4$ nanoparticles within the shell allowed for greater light absorption; and (3) the above two aspects led to a rapid charge transfer at the interface between Co$_3$O$_4$ and CuO. Thus, with active interfaces and a thin shell assisting in reduced charge scattering, sample #2B is excited with visible light without H$_2$O$_2$ and resulted in charge carrier generation with less scattering and rapid separation, both responsible for higher η (∼67.5%). However, this η was still lower than when the UV illumination was supplemented with H$_2$O$_2$. It must be noted that there exists a good lattice match between the CuO nanowire and Co$_3$O$_4$ shell at the interface of the nanowire heterostructures (Figure S10). However, in the case of nanowire heterostructures with a thick Co$_3$O$_4$ shell, in addition to the good interfacial lattice relationship and assuming that charge transfer is occurring at the interface, the generated charge carriers will still undergo scattering and recombination in the thick Co$_3$O$_4$ shell. So, in regard to photodegradation using nanowire heterostructures composed of a thick Co$_3$O$_4$ shell, the dominant role must be played by Co$_3$O$_4$ necessitating the use of a sacrificial agent to aid in the charge separation process.

To further explain these aspects, the band gap diagrams and electron−hole separation and recombination in both the components (CuO and Co$_3$O$_4$) were analyzed. Considering that CuO has an average band gap energy of ∼1.35 eV, it could exhibit transitions from the valence band and/or from the O^{2-} band to the conduction band. The latter is consistent with band gap energy of ∼3.25 eV.[71] For Co$_3$O$_4$, transitions from O^{2-} to Co^{3+} and/or Co^{2+} are known with average band gaps of ∼1.5 and ∼2.0 eV.[67] By aligning the O^{2-} band edge in CuO and Co$_3$O$_4$, relative band edge positions of CuO and Co$_3$O$_4$ were determined and a combined band energy diagram for CuO−Co$_3$O$_4$ nanowire heterostructures was derived in Figure 11b. The interaction of semiconducting oxide components under illumination and H$_2$O$_2$ generated electron−hole pairs which assisted in carrying out phenol photodegradation (Figure 11c). These electrons and holes have a greater tendency to combine rather than participate in a photochemical reaction in the case of the thick polycrystalline Co$_3$O$_4$ shell necessitating the use of H$_2$O$_2$ to achieve phenol photodegradation (Figure 11b, schematic on the right). It is proposed here that O^{2-} to Co^{2+}/Co^{3+} transitions were more dominant in samples with a thick polycrystalline Co$_3$O$_4$ shell. This is also true as we observed that Co$_3$O$_4$ nanotubes showed comparable photocatalytic efficiencies with sample #4B (Table S4). On the other hand, the morphology of sample #2B has more active interfaces, where O^{2-} to Co^{2+} transitions (within the Co$_3$O$_4$ shell and embedded nanoparticles) and CuO photoactivity couple together to result in anomalously high η (Figure 11b, schematic on the left). Since the conduction band of Co$_3$O$_4$

5604

dx.doi.org/10.1021/am301488c | ACS Appl. Mater. Interfaces 2012, 4, 5590−5607

(Co^{2+}) is slightly higher than the valence band of CuO, it is possible that, after illumination, this could effectively extend the lifetime of electrons in CuO and holes in Co_3O_4, which greatly increased the η.

The degradation conditions of visible light illumination with H_2O_2 were selected further for photodegradation kinetics (Figure 12). A first-order kinetics was observed as shown by
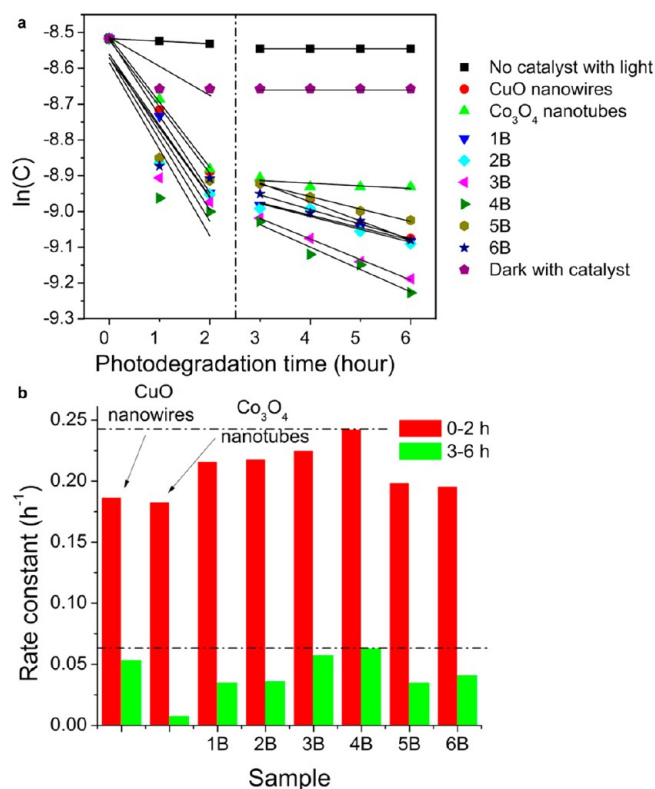

Figure 12. Phenol photodegradation kinetics study. (a) First-order kinetics (linear fitting) of photodegradation behavior for various photocatalysts and rate constants (b). Note: These data are obtained from Figure 10b, and the photodegradation reaction was performed under visible illumination with H_2O_2.

linear relationship between ln C and t (C is the phenol concentration at time t, Figure 12a and Table S5).[72] For control as well as nanowire heterostructure samples, the photodegradation process was much faster (~20 to 50 times, Figure 12b) in the first 2 h and slowed down for the next 4 h. Considering only a small amount (0.02 mM, 12 μL) of sacrificial agent (H_2O_2) was added, the sharp decrease resulted from the depletion of H_2O_2, which assisted in absorbing photogenerated electrons and suppressed the recombination process.[73] Thus, it is necessary to divide the photodegradation process under these conditions into two parts; one between 0 and 2 h and other between 3 and 6 h. The region between 2 and 3 h could be considered as the transition zone, where H_2O_2 is nearly finished. The rate constants of reactions using different photocatalysts were compared in Figure 12b and showed that the nanowire heterostructures displayed better performance (with sample #4B ranking highest) than individual components (CuO nanowires and Co_3O_4 nanotubes).

4. CONCLUSIONS

Novel CuO−Co_3O_4 nanowire heterostructures were successfully fabricated in a dry processing route in a line-of-sight

sputter deposition of Co onto standing CuO nanowires and subsequent thermal annealing. Three-fold fundamental understanding was developed in this study. In the first part of the study, morphological evolution, deposition kinetics, and nanomechanical aspects of the CuO−Co nanowire heterostructures were studied. The diameter of CuO−Co nanowire heterostructures showed a linear trend in the initial 10 min (Stranski−Krastanov mode) and a quadratic fit beyond. The latter was attributed to low Co diffusion on the columnar grain surface because of kinetic roughening. Theoretical analysis revealed that the alignment of the nanowire and Co surface migration played a dominant role in uniformly coating the CuO nanowires. Microscopic observation and FEM analysis proved that the vertical alignment of nanowires was critical for minimizing the von Mises equivalent stress distributions, bending of nanowires, and self-shadowing effects. In the second part of the study, air annealing of CuO−Co nanowire heterostructures resulted in Co_3O_4 with different morphologies (from nanoparticles to polycrystalline shells) and controlled interfaces. This was studied as a function of sputtering and air-annealing duration. Heterostructures remained standing on the substrate, and faceted nanoparticles or islands of Co_3O_4 evolved with prolonged annealing. Core CuO nanowires were then selectively etched to result in polycrystalline Co_3O_4 nanotubes, which also confirmed a uniform polycrystalline Co_3O_4 shell. In the third and final part of the study, standing CuO−Co_3O_4 nanowire heterostructures exhibited multiple absorption edges (UV to visible range) and band gap energies ranging from ~1.1 to 3.0 eV. Photodegradation of phenol as a function of heterostructure morphology and composition, illumination wavelength, and presence/absence of sacrificial agent (H_2O_2) was studied. A thick polycrystalline Co_3O_4 shell (~50 nm) on CuO nanowires showed optimized photodegradation behavior (η ~50−90%) in a low-powered (8 W) UV or visible light illumination with H_2O_2. However, CuO nanowires coated with a thin (<10 nm) Co_3O_4 shell with embedded nanoparticles showed an anomalously high η (~67.5%) under visible light without H_2O_2. It is, therefore, proposed that the morphology and interfaces of CuO−Co_3O_4 nanowire heterostructures strongly affect charge transfer or separation mechanisms, allowing modulation of their photodegradation performance. Such unique nanowire heterostructures reflect the potential of these oxides with well-controlled morphologies as universal photocatalysts.

■ ASSOCIATED CONTENT

Ⓢ Supporting Information

Sputtering mean free path calculations, number of Co species per nanowire per second and impinging velocity calculations, momentum conservation calculations in x' and y', estimation of $m_{CuO/Co}$, tables for systematic growth study, diameter of nanowires, projection area of nanoparticles, efficiencies and kinetic fitting of photodegradation, SEM images of CuO nanowires and CuO−Co nanowire heterostructures, length and tilting angle distribution of CuO nanowires, SEM images of aligned and standing CuO−Co nanowire heterostructures, TEM images showing tilting of nanowire and formation of columnar structures on nanowire, stress field of nanowires with different bending angles, HR-TEM of interfaces and Raman depth profiling of nanowire heterostructures, theoretical calculation of oxides shell thickness, SEM images of Co_3O_4 nanotubes anchored on the substrate, UV−vis spectrum of phenol solution, and absorbance vs wavelength and Tauc plots

for different samples. This material is available free of charge via the Internet at http://pubs.acs.org.

■ AUTHOR INFORMATION

Corresponding Author

*E-mail: nchopra@eng.ua.edu. Phone: 205-348-4153. Fax: 205-348-2164.

Notes

The authors declare no competing financial interest.

■ REFERENCES

(1) Mann, S. *Nat. Mater.* **2009**, *8*, 781−792.

(2) Kamat, P. V. *J. Phys. Chem. C* **2007**, *111*, 2834−2860.

(3) Fu, J. X.; He, Y. P.; Zhao, Y. P. *IEEE Sens. J.* **2008**, *8*, 989−997.

(4) Bierman, M. J.; Jin, S. *Energy Environ. Sci.* **2009**, *2*, 1050−1059.

(5) Eymery, G.; Biasiol, J.; Kapon, E.; Ogino, T. *C. R. Phys.* **2005**, *6*, 105−116.

(6) Grimes, C. A.; Varghese, O. K.; Ranjan, S. K. *Light, Water, and Hydrogen: The Solar Generation of Hydrogen by Water Photoelectrolysis*; Springer: New York, 2008.

(7) Baxter, J. B.; Aydil, E. S. *Appl. Phys. Lett.* **2005**, *86*, 053114.

(8) Zhou, W.; Cheng, C.; Liu, J.; Tay, Y. Y.; Jiang, J.; Jia, X.; Zhang, J.; Gong, H.; Hng, H. H.; Fan, H. J. *Adv. Funct. Mater.* **2011**, *21*, 2439−2445.

(9) Hill, J. J.; Banks, N.; Haller, K.; Orazem, M. E.; Ziegler, K. J. *J. Am. Chem. Soc.* **2011**, *133*, 18663−18672.

(10) Musin, R. N.; Wang, X. Q. *Phys. Rev. B* **2005**, *71*, 155318.

(11) Yang, D.; Liu, H.; Zheng, Z.; Yuan, Y.; Zhao, J. C.; Waclawik, E. R.; Ke, X.; Zhu, H. *J. Am. Chem. Soc.* **2009**, *131*, 17885−17893.

(12) Paola, A. D.; Palmisano, L.; Augugliaro, V. *Catal. Today* **2000**, *58*, 141−149.

(13) Pan, P. W.; Chen, Y. W. *Catal. Commun.* **2007**, *8*, 1546−1549.

(14) Barreca, D.; Fornasiero, P.; Gasparotto, A.; Gombac, V.; Maccato, C.; Montini, T.; Tondello, E. *Chem. Sus. Chem.* **2009**, *2*, 230−233.

(15) Xia, X. H.; Tu, J. P.; Zhang, Y. Q.; Wang, X. L.; Gu, C. D.; Zhao, X. B.; Fan, H. J. *ACS Nano* **2012**, *6*, 5531−5538.

(16) Kemell, M.; Harkonen, E.; Pore, V.; Ritala, M.; Leskela, M. *Nanotechnology* **2010**, *21*, 035301.

(17) Zhang, H.; Luo, X.; Xu, J.; Xiang, B.; Yu, D. *J. Phys. Chem. B* **2004**, *108*, 14866−14869.

(18) Chopra, N. *Mater. Technol.* **2010**, *25*, 212−230.

(19) Shahida, M.; Shakira, I.; Yang, S. J.; Kang, D. J. *Mater. Chem. Phys.* **2010**, *124*, 619−622.

(20) Chueh, Y. L.; Hsieh, C. H.; Chang, M. T.; Chou, L. J.; Lao, C. S.; Song, J. H.; Gan, J. Y.; Wang, Z. L. *Adv. Mater.* **2007**, *19*, 143−149.

(21) Feng, Y.; Cho, I. S.; Rao, P. M.; Cai, L.; Zheng, X. *Nano Lett.* **2012**, DOI: 10.1021/nl300060b

(22) Chun, J.; Lee, J. *Eur. J. Inorg. Chem.* **2010**, *27*, 4251−4263.

(23) Tak, Y.; Hong, S. J.; Lee, J. S.; Yong, K. J. *J. Mater. Chem.* **2009**, *19*, 5945−5951.

(24) Shi, W.; Chopra, N. *J. Nanopart. Res.* **2011**, *13*, 851−868.

(25) Zhao, X.; Wang, P.; Li, B. *Chem. Commun.* **2010**, *46*, 6768−6770.

(26) Wolf, S.; Tauber, R. N. *Silicon Processing for the VLSI Era*; Lattice Press: Sunset Beach, CA, 1999.

(27) Li, L.; Koshizaki, N. *J. Mater. Chem.* **2010**, *20*, 2972−2978.

(28) Han, S.; Zhang, D.; Zhou, C. *Appl. Phys. Lett.* **2006**, *88*, 133109.

(29) LaForge, J. M.; Taschuk, M. T.; Brett, M. J. *Thin Solid Films* **2011**, *519*, 3530−3537.

(30) Huang, J. H.; Chen, C. Y.; Lai, Y. F.; Shih, Y. I.; Lin, Y. C.; He, J. H.; Liu, C. P. *Cryst. Growth Des.* **2010**, *10*, 3297−3301.

(31) Noh, J. S.; Lee, M. K.; Ham, J.; Lee, W. *Nanoscale Res. Lett.* **2011**, *6*, 598.

(32) Shi, W.; Chopra, N. *Mater. Res. Soc. Res. Proc.* **2010**, *1256*, 1256-N10-03.

(33) Gasparotto, A.; Barreca, D.; Bekermann, D.; Devi, A.; Fischer, R. A.; Fornasiero, P.; Gombac, V.; Lebedev, O. L.; Maccato, C.; Montini, T.; Tendeloo, G. V.; Tondello, E. *J. Am. Chem. Soc.* **2011**, *133*, 19362−19365.

(34) Maeda, K.; Ohno, T.; Domen, K. *Chem. Sci.* **2011**, *2*, 1362−1368.

(35) Jiang, X.; Herricks, T.; Xia, Y. *Nano Lett.* **2002**, *2*, 1333−1338.

(36) Kaito, C.; Nakata, Y.; Saito, Y.; Naiki, T.; Fujita, K. *J. Cryst. Growth* **1986**, *74*, 469−479.

(37) Cao, G. *Nanostructure and Nanomaterials*; Imperial College Press: London, U.K., 2004.

(38) Tunc, I.; Bruns, M.; Liemann, H. G.; Grunze, M.; Koelsch, P. *Surf. Interface Anal.* **2010**, *42*, 835−841.

(39) Chopra, N.; Hu, B.; Hinds, B. J. *J. Mater. Res.* **2007**, *22*, 2691−2699.

(40) Shen, Y.; Hong, J. I.; Peng, Z.; Fang, H.; Zhang, S.; Dong, S.; Snyder, R. L.; Wang, Z. L. *J. Phys. Chem. C* **2010**, *114*, 21277−21280.

(41) Chen, L. J. *Mater. Sci. Eng., R* **2000**, *29*, 115−152.

(42) Gilmer, G. H.; Huang, H.; Roland, C. *Mater. Sci.* **1998**, *12*, 354−380.

(43) Martin, L. W.; Chu, Y. H.; Ramesh, R. *Mater. Sci. Eng., R.* **2010**, *68*, 89−133.

(44) Chung, B. X.; Liu, C. P. *Mater. Lett.* **2004**, *58*, 1437−1440.

(45) Kaune, G.; Ruderer, M. A.; Metwalli, E.; Couet, S.; Schlage, K.; Rohlsberger, R.; Roth, S. V.; Muller-Buschbaum, P. *ACS Appl. Mater. Interfaces* **2009**, *1*, 353−360.

(46) Petrov, I.; Barna, P. B.; Hultman, L.; Greene, J. E. *J. Vac. Sci. Technol., A* **2005**, *21*, S117−S128.

(47) Toku, Y.; Muraoka, M. *Nanosci. Nanotechnol. Lett.* **2010**, *2*, 197−202.

(48) Ohring, M. *Materials Science of Thin Films*, 2nd ed.; Academic Press: Waltham, MA, 2001.

(49) Granqvist, C. G. *Sol. Energy Mater. Sol. Cells* **2012**, *99*, 166−175.

(50) Li, C.; Hsieh, J. H. *Thin Solid Films* **2002**, *475*, 102−108.

(51) Mahieu, S.; Aeken, K. V.; Depla, D.; Smeets, D.; Vantomme, A. *J. Phys. D: Appl. Phys.* **2008**, *41*, 152005.

(52) Tan, E. P. S.; Zhu, Y.; Yu, T.; Dai, L.; Sow, C. H.; Tan, V. B. C.; Lim, C. T. *Appl. Phys. Lett.* **2007**, *90*, 163112.

(53) Zhang, D. F.; Breguet, J. M.; Clavel, R.; Philippe, L.; Utke, I.; Michler, J. *Nanotechnology* **2009**, *20*, 365706.

(54) Chen, C. Q.; Shi, Y.; Zhang, Y. S.; Zhu, J.; Yan, Y. *J. Phys. Rev. Lett.* **2006**, *96*, 075505.

(55) http://www.csc.fi/english/pages/elmer/.

(56) Asthana, A.; Momeni, K.; Prasad, A.; Yap, Y. K.; Yassar, R. S. *Nanotechnology* **2011**, *22*, 265712.

(57) Ribbens, S.; Beyers, E.; Schellens, K.; Mertens, M.; Ke, X.; Bals, S.; Tendeloo, G. V.; Meynen, V.; Cool, P. *Microporous Mesoporous Mater.* **2012**, *156*, 62−72.

(58) Haynes, W. M. *CRC Handbook of Chemistry and Physics*; CRC Press: Boca Raton, FL, 2012.

(59) Chou, M. H.; Liu, S. B.; Huang, C. Y.; Wu, S. Y.; Cheng, C. L. *Appl. Surf. Sci.* **2008**, *254*, 7539−7543.

(60) Tyczkowski, J.; Kapica, R.; Lojewska, J. *Thin Solid Films* **2007**, *515*, 6590−6595.

(61) Gouadec, G.; Colomban, P. *Prog. Cryst. Growth Charact. Mater.* **2007**, *53*, 1−56.

(62) Maruyama, Y.; Kanematsu, W. *J. Appl. Phys.* **2011**, *110*, 103107.

(63) Kingery, W. D.; Bowen, H. K.; Uhlmann, D. R. *Introduction to Ceramics*; John Wiley & Sons: New York, 1997.

(64) Cao, L.; Garipcan, B.; Atchison, J. S.; Ni, C.; Nabet, B.; Spanier, J. E. *Nano Lett.* **2006**, *6*, 1852−1857.

(65) Anandan, S.; Wen, X.; Yang, S. *Mater. Chem. Phys.* **2005**, *93*, 35−40.

(66) Gu, F.; Li, C.; Hu, Y.; Zhang, L. *J. Cryst. Growth* **2007**, *304*, 369−373.

(67) Barreca, D.; Massignan, C.; Daolio, S.; Fabrizio, M.; Piccirillo, C.; Armelao, L.; Tondello, E. *Chem. Mater.* **2001**, *13*, 588−593.

(68) Banerjee, R.; Jayakrishnan, R.; Ayyub, P. *J. Phys.: Condens. Matter* **2000**, *12*, 10647−10654.

(69) Barakat, N. A. M.; Khil, M. S.; Sheikh, F. A.; Kim, H. Y. *J. Phys. Chem. C* **2008**, *112*, 12225−12233.

(70) Long, M.; Cai, W.; Cai, J.; Zhou, B.; Chai, X.; Wu, Y. *J. Phys. Chem. B* **2006**, *110*, 20211−20216.

(71) Koffyberg, F. P.; Benko, F. A. *J. Appl. Phys.* **1982**, *53*, 1173−1177.

(72) Zhang, F.; Zhao, J.; Shen, T.; Hidaka, H.; Pelizzetti, E.; Serpone, N. *Appl. Catal., B* **1998**, *15*, 147−156.

(73) Cornish, B. J. P. A.; Lawton, L. A.; Robertson, P. K. *J. Appl. Catal., A* **2000**, *25*, 59−67.